The Planetary Science Journal, 6:114 (23pp), 2025 May https://doi.org/10.3847/PSJ/adcab3

Seasonal Evolution of Titan's Stratospheric Tilt and Temperature Field at High Resolution from Cassini/CIRS

Lucy Wright[1], Nicholas A. Teanby[1], Patrick G. J. Irwin[2], Conor A. Nixon[3], Nicholas A. Lombardo[4], Juan M. Lora[4], and Daniel Mitchell[5]
[1] School of Earth Sciences, University of Bristol, Bristol, UK
[2] Atmospheric, Oceanic, and Planetary Physics, Department of Physics, University of Oxford, Oxford, UK
[3] Planetary Systems Laboratory, NASA Goddard Space Flight Center, Greenbelt, MD 20771, USA
[4] Department of Earth and Planetary Sciences, Yale University, New Haven, CT 06511, USA
[5] School of Geographical Sciences, University of Bristol, Bristol, UK
Received 2025 January 24; revised 2025 March 22; accepted 2025 April 7; published 2025 May 20

Abstract

The Cassini spacecraft observed Titan from 2004 to 2017, capturing key atmospheric features, including the tilt of the middle atmosphere and the formation and breakup of winter polar vortices. We analyze low spectral resolution infrared observations from Cassini's Composite Infrared Spectrometer (CIRS), which provide excellent spatial and temporal coverage and the best horizontal spatial resolution of any of the CIRS observations. With approximately 4 times higher meridional resolution than previous studies, we map the stratospheric temperature for almost half a Titan year. We determine the evolution of Titan's stratospheric tilt, finding that it is most constant in the inertial frame, directed $120° \pm 6°$ west of the Titan–Sun vector at the northern spring equinox, with seasonal oscillations in the tilt magnitude between around $2.^{\circ}5$ and 8°. Using the high meridional resolution temperature field, we reveal finer details in the zonal wind and potential vorticity. In addition to the strong winter zonal jet, a weaker zonal jet in Titan's summer hemisphere is observed, and there is a suggestion that the main winter hemisphere jet briefly splits into two. We also present the strongest evidence yet that Titan's polar vortex is annular for part of its life cycle.

Unified Astronomy Thesaurus concepts: Titan (2186); Radiative transfer (1335); Infrared spectroscopy (2285); Planetary atmospheres (1244)

1. Introduction

Titan, the largest moon of Saturn, hosts a nitrogen-rich atmosphere with complex organic chemistry, making it one of the most intriguing bodies in the solar system. Its middle atmosphere comprises around 98% nitrogen (N_2) and 1%–1.5% methane (CH_4) (H. B. Niemann et al. 2010). Photochemical reactions in Titan's upper atmosphere drive the formation of complex hydrocarbons (C_xH_y) and nitriles ($C_xH_yN_z$) (E. H. Wilson 2004; P. Lavvas et al. 2008; M. Dobrijevic et al. 2014; J. Loison et al. 2015; V. Vuitton et al. 2019; C. A. Nixon 2024), which serve as tracers of atmospheric dynamics. Titan's atmosphere exhibits many dynamical features similar to Earth's. Titan is therefore an excellent natural laboratory for testing dynamical and photochemical models of Earth's atmosphere and can act as an analog for understanding organic-rich prebiotic environments beyond our solar system. The Cassini spacecraft, during its 13 yr mission from 2004 July ($L_s = 293°$) to 2017 September ($L_s = 93°$), conducted extensive observations of Titan that revealed the moon's complex stratospheric dynamics. Cassini performed 127 close fly-bys of Titan spanning almost half of its year, from northern midwinter through to the northern summer solstice.

Due to Titan's tidal locking to Saturn, and Saturn's obliquity of $26.^{\circ}7$, comparable to Earth's $23.^{\circ}5$, Titan experiences strong seasonal effects. General circulation models (GCMs) predict the circulation in Titan's stratosphere and mesosphere to be dominated by a single pole-to-pole circulation cell for most of its year, with an ascending branch at the summer pole and a descending branch at the winter pole (F. Hourdin et al. 1995; P. Rannou et al. 2004; C. E. Newman et al. 2011; S. Lebonnois et al. 2012; N. A. Lombardo & J. M. Lora 2023b), consistent with Cassini observations (F. M. Flasar et al. 2005; R. K. Achterberg et al. 2008a; N. A. Teanby et al. 2008). The circulation is predicted to reverse direction shortly after Titan's equinox, with two circulation cells existing for approximately 2 Earth years during the transition, consistent with observations (e.g., N. A. Teanby et al. 2012; S. Vinatier et al. 2015).

Seasonal variations also produce significant thermal gradients, with middle-atmosphere polar temperatures observed to be around 10–30 K, but up to 50 K, cooler than the equator (N. A. Teanby et al. 2017; C. Mathé et al. 2020; S. Vinatier et al. 2020; R. K. Achterberg 2023). Horizontal thermal gradients drive the formation of a strong circumpolar jet or polar vortex around Titan's winter pole (F. M. Flasar et al. 2005; N. Teanby et al. 2006; R. K. Achterberg et al. 2008a), which acts as a barrier to mixing of polar and midlatitude air. Polar vortices are observed in nearly all planetary atmospheres in our solar system and are often the location of key atmospheric processes, such as CO_2 condensation on Mars (A. Colaprete et al. 2008) and ozone depletion on Earth (D. M. Mitchell et al. 2021). Titan's polar vortex is typically characterized by (1) increased trace gas abundance in the vortex (N. A. Teanby et al. 2008; N. Teanby et al. 2009a, 2009b; A. Coustenis et al. 2010; S. Vinatier et al. 2010) as the subsiding branch of the meridional circulation transports trace gases downward and the strong circumpolar winds act as a mixing barrier, effectively trapping the trace gases in the vortex (F. M. Flasar et al. 2005; N. Teanby et al. 2006; A. Coustenis et al. 2007; N. A. Teanby et al. 2008); (2) a

cold lower stratosphere (R. K. Achterberg et al. 2008b; N. A. Teanby et al. 2008; R. K. Achterberg et al. 2011; A. E. Thelen et al. 2024) due to increased trace gas long-wave cooling and lack of insolation; and (3) a hot stratopause (R. K. Achterberg et al. 2008b, 2011; N. A. Teanby et al. 2008; A. E. Thelen et al. 2024) caused by adiabatic heating of the subsiding branch. Potential vorticity (PV) is a key quantity in diagnosing the dynamics of a planetary atmosphere, and previous studies have used PV to study Titan's polar vortices (R. K. Achterberg et al. 2008b, 2011; N. A. Teanby et al. 2008; J. Sharkey et al. 2021), as a strong PV gradient can indicate a mixing barrier and can therefore be used to probe a vortex edge. Despite this configuration tending to be dynamically unstable (L. Rayleigh 1879; D. G. Dritschel 1986), there are some observations that suggest that Titan's polar vortex is annular in shape. N. A. Teanby et al. (2008), R. K. Achterberg et al. (2011), and J. Sharkey et al. (2021) observe opposing PV gradients encircling the winter pole, hinting that the vortex has an outer edge but also an inner edge, forming an annulus around the pole. Observation of Titan's polar vortices is not possible from Earth-based observatories, due to solar system geometry. The Cassini spacecraft performed high orbital inclination phases, observing the breakdown of Titan's north polar vortex during northern winter (before 2009 September, $L_s < 0°$) and the formation of the south polar vortex in northern spring (after 2009 September, $L_s > 0°$).

Titan's entire stratosphere is in superrotation, meaning that zonal wind speeds are much faster than the rotation of the solid body (P. L. Read 1986; P. L. Read & S. Lebonnois 2018). This phenomenon is known to also exist in the atmosphere of Venus. Titan's superrotating winds have been observed through submillimeter Doppler wind measurements (R. Moreno et al. 2005; E. Lellouch et al. 2019; M. A. Cordiner et al. 2020; S. Light et al. 2024) and temperature measurements (R. K. Achterberg et al. 2008a, 2011; N. A. Teanby et al. 2008; J. Sharkey et al. 2021) and are reproduced in GCMs (C. E. Newman et al. 2011; S. Lebonnois et al. 2012; N. T. Lewis et al. 2023; N. A. Lombardo & J. M. Lora 2023b, 2023a). Titan's stratosphere rotates about an axis offset from Titan's solid-body rotation axis by around 4°. This so-called "stratospheric tilt" was first noted by R. K. Achterberg et al. (2008a), from zonal temperature distributions derived from early Cassini/Composite Infrared Spectrometer (CIRS) observations. Broadly consistent stratospheric tilt magnitudes have since been determined through further temperature measurements (R. K. Achterberg et al. 2011) and composition retrievals (N. Teanby et al. 2010; J. Sharkey et al. 2020) and by analysis of images of stratospheric haze (M. T. Roman et al. 2009; N. W. Kutsop et al. 2022; A. S. Vashist et al. 2023) and polar clouds (R. A. West et al. 2016). However, the mechanism causing this tilt is not yet understood. Early observations of the tilt (R. K. Achterberg et al. 2008a; M. T. Roman et al. 2009; N. Teanby et al. 2010) determine the tilt axis to have a direction that is constant in the solar-fixed frame (constant with respect to the Titan–Sun vector), suggesting that the tilt is a result of solar-induced dynamics. However, more recent studies that include observations later in Titan's northern winter (R. K. Achterberg et al. 2011; 2004–2009), and into northern spring (J. Sharkey et al. 2020; C. Snell & D. Banfield 2024; 2004–2017) suggest that the tilted axis is more consistent in the "inertial"- or solar-system-fixed frame—that is, constant with respect to the Titan–Sun vector at Titan's northern spring equinox—and hence is not solely a response to incident solar heating. Consequently, the question whether Titan's stratospheric tilt remains fixed in any frame remains inconclusive. Understanding the cause of Titan's stratospheric tilt may give insight into the underlying dynamics that drive Titan's stratospheric superrotation and superrotating atmospheres in general.

The CIRS instrument (F. M. Flasar et al. 2004; D. E. Jennings et al. 2017; C. A. Nixon et al. 2019), one of the 12 instruments on board Cassini, observed Titan in the infrared (IR). L. Wright et al. (2024) show that it is possible to accurately determine temperature and composition from high spatial resolution (low spectral resolution) CIRS observations. Here we use CIRS observations spanning the full Cassini mission (2004–2017) to improve the temporal and spatial resolution of Titan's stratospheric temperature field. The temperature meridional resolution in this study is 2°, around 4–7× higher resolution than in previous CIRS studies (R. K. Achterberg et al. 2011; J. Sharkey et al. 2021), enabling the preservation of finer features in the mean zonal wind field and PV distribution. This increased resolution allows for more accurate constraints on the shape, size, and structure of Titan's winter polar vortices. The high signal-to-noise ratio (S/N) also means that we can bin in 1-Earth-year bins, providing the best full-mission temporal resolution to study the seasonal changes of Titan's stratosphere, including the formation and breakup of Titan's winter polar vortices. GCMs are powerful tools in understanding the forcing behind observed atmospheric dynamics. We compare our observed temperatures and determined zonal winds with those simulated by the Titan Atmospheric Model (TAM) GCM (J. M. Lora et al. 2015; N. A. Lombardo & J. M. Lora 2023b, 2023a). Additionally, we use the deduced high meridional resolution temperature field to comprehensively explore the variation in Titan's stratospheric tilt. A limitation of previous Cassini/CIRS studies of the tilt is that they estimate a mean position of the tilt axis over all or part of the mission time frame (R. K. Achterberg et al. 2008a; M. T. Roman et al. 2009; N. Teanby et al. 2010; R. A. West et al. 2016; J. Sharkey et al. 2020). Here we extend the previous analyses by determining a time series of the tilt axis over the entire Cassini mission (2004–2017), to investigate the seasonal dependence of Titan's stratospheric tilt. We determine the mean tilt axis for each Earth-year period in the mission time frame by examining the zonal symmetry of the stratospheric temperature field. A time series of the tilt has been considered previously using Cassini/CIRS observations (R. K. Achterberg et al. 2011), although only considering a short period of observations (2004–2009). The time dependence of the tilt axis has also been estimated using observations of Titan's haze annuli (N. W. Kutsop et al. 2022) acquired by Cassini's Visible and Infrared Mapping Spectrometer (VIMS), although this probes lower altitudes than the CIRS nadir observations we use here. Both studies will provide a valuable comparison to our results.

2. Data

To determine the temperature distribution in Titan's stratosphere, we use IR spectra measured by Cassini/CIRS (F. M. Flasar et al. 2004; D. E. Jennings et al. 2017; C. A. Nixon et al. 2019). We use 85 nadir mapping sequences from 70 fly-bys over a 13 yr period (2004–2017), listed in

Table 1
The CIRS Observation Sequences Used in This Study

CIRS Observation	Date	L_s (deg)	Longitude (deg W)	FWHM (cm^{-1})	FP4 N	FP4 FOV (deg)
CIRS_005TI_FIRNADCMP005_UVIS	01/04/2005	303.1	−148.1	14.56	4419	0.550000
CIRS_006TI_FIRNADMAP003_UVIS	17/04/2005	303.7	28.5	14.51	6899	0.930000
CIRS_00BTI_FIRNADMAP001_UVIS	13/12/2004	299.1	160.3	14.56	12886	1.190000
CIRS_013TI_FIRNADMAP002_PRIME	22/08/2005	308.4	26.2	14.56	6425	0.620000
CIRS_019TI_FIRNADMAP005_UVIS	27/12/2005	313.1	−158.5	14.20	4624	1.030000
CIRS_020TI_FIRNADCMP004_UVIS	16/01/2006	313.8	−7.6	14.20	9377	1.090000
CIRS_021TI_FIRNADMAP003_UVIS	28/02/2006	315.4	−147.6	14.20	7178	1.340000
CIRS_023TI_FIRNADMAP003_UVIS	01/05/2006	317.6	−133.1	14.20	5687	1.540000
CIRS_024TI_FIRNADMAP002_UVIS	20/05/2006	318.4	155.8	14.20	9177	0.970000
CIRS_024TI_FIRNADMAP003_PRIME	21/05/2006	318.4	−16.4	14.20	3440	0.580000
CIRS_026TI_FIRNADMAP003_PRIME	22/07/2006	320.6	−20.8	14.20	2895	0.590000
CIRS_035TI_MONITORNA001_ISS	13/12/2006	325.9	−11.7	14.20	2552	1.760000
CIRS_036TI_FIRNADMAP002_PRIME	28/12/2006	326.4	124.4	14.20	7668	0.690000
CIRS_036TI_FIRNADMAP003_PRIME	28/12/2006	326.4	−29.1	14.20	5315	0.750000
CIRS_037TI_GLOBMAP001_ISS	13/01/2007	327.0	−39.6	14.20	14505	1.230000
CIRS_038TI_FIRNADMAP002_PRIME	29/01/2007	327.6	−51.1	14.20	1359	0.840000
CIRS_038TI_HIRESNAC001_VIMS	29/01/2007	327.6	−26.4	14.20	3955	0.110000
CIRS_040TI_FIRNADMAP001_PRIME	10/03/2007	328.9	44.1	14.20	6987	0.670000
CIRS_040TI_FIRNADMAP002_PRIME	10/03/2007	328.9	−141.7	14.20	2750	0.790000
CIRS_041TI_EUVFUV002_UVIS	26/03/2007	329.5	−127.4	14.20	6774	1.180000
CIRS_043TI_FIRNADMAP001_PRIME	26/04/2007	330.6	29.3	14.18	6913	0.630000
CIRS_045TI_EUVFUV001_UVIS	28/05/2007	331.8	21.4	14.20	9972	1.190000
CIRS_046TI_FIRNADMAP902_PRIME	14/06/2007	332.4	−148.4	14.20	7068	0.610000
CIRS_048TI_EUVFUV001_UVIS	18/07/2007	333.6	147.3	14.20	5509	1.040000
CIRS_049TI_FIRNADMAP001_PRIME	31/08/2007	335.2	22.0	14.20	3701	0.600000
CIRS_050TI_EUVFUV001_UVIS	01/10/2007	336.3	11.6	14.20	4206	1.240000
CIRS_052TI_FIRNADMAP001_PRIME	18/11/2007	338.0	21.2	14.18	7542	0.610000
CIRS_053TI_FIRNADMAP001_PRIME	04/12/2007	338.6	25.0	14.18	7459	0.670000
CIRS_055TI_FIRNADMAP002_PRIME	06/01/2008	339.7	−135.6	14.18	3129	0.850000
CIRS_062TI_FIRNADMAP002_PRIME	25/03/2008	342.6	−139.4	14.18	2988	0.810000
CIRS_069TI_EUVFUV001_UVIS	28/05/2008	344.8	58.1	14.18	6104	1.110000
CIRS_093TI_FIRNADMAP002_PRIME	20/11/2008	350.9	−105.8	14.18	7643	0.640000
CIRS_095TI_EUVFUV001_UVIS	06/12/2008	351.5	−92.9	14.18	3554	1.220000
CIRS_107TI_FIRNADMAP002_PRIME	28/03/2009	355.3	−122.7	14.18	4129	0.630000
CIRS_108TI_FIRNADMAP002_PRIME	04/04/2009	355.6	−86.4	14.18	5100	0.550000
CIRS_109TI_FIRLMBAER002_PRIME	20/04/2009	356.1	−158.9	14.17	334	0.190000
CIRS_110TI_FIRNADMAP001_PRIME	06/05/2009	356.7	79.7	14.18	7923	0.600000
CIRS_111TI_FIRNADMAP002_PRIME	22/05/2009	357.2	−101.9	14.18	6635	0.640000
CIRS_113TI_EUVFUV001_UVIS	23/06/2009	358.3	124.2	14.18	9109	1.190000
CIRS_113TI_EUVFUV002_UVIS	23/06/2009	358.3	−38.7	14.18	6428	1.360000
CIRS_114TI_EUVFUV001_UVIS	09/07/2009	358.9	131.6	14.18	9006	1.000000
CIRS_115TI_FIRNADMAP002_PRIME	25/07/2009	359.4	−29.6	14.18	3006	0.710000
CIRS_119TI_EUVFUV002_UVIS	13/10/2009	2.1	−19.2	14.18	4021	1.390000
CIRS_123TI_FIRNADMAP001_PRIME	28/12/2009	4.7	15.7	14.18	7054	0.670000
CIRS_138TI_EUVFUV002_UVIS	25/09/2010	13.8	−153.5	14.16	3870	1.400000
CIRS_148TI_EUVFUV001_UVIS	09/05/2011	21.3	−14.2	14.16	4356	1.100000
CIRS_149TI_FIRNADMAP002_PRIME	21/06/2011	22.7	−140.4	14.16	3505	0.550000
CIRS_161TI_FIRLMBT001_PRIME	19/02/2012	30.5	149.5	14.15	608	0.140000
CIRS_161TI_FIRNADMAP001_PRIME	19/02/2012	30.5	149.7	14.16	8452	0.740000
CIRS_161TI_FIRNADMAP002_PRIME	19/02/2012	30.6	−33.8	14.16	8900	0.690000
CIRS_169TI_FIRLMBT001_PRIME	25/07/2012	35.6	118.5	14.16	231	0.040000
CIRS_169TI_FIRNADMAP002_PRIME	25/07/2012	35.6	−156.0	14.16	8231	0.570000
CIRS_175TI_FIRLMBT001_PRIME	30/11/2012	39.7	109.5	14.17	211	0.060000
CIRS_185TI_FIRNADMAP001_PRIME	06/04/2013	43.7	48.6	14.18	3483	0.630000
CIRS_197TI_HIRES001_ISS	12/09/2013	48.7	78.1	14.20	4360	0.280000
CIRS_197TI_HIRES001_VIMS	12/09/2013	48.7	−144.3	14.20	6080	0.060000
CIRS_199TI_FIRLMBAER002_PRIME	01/12/2013	51.2	150.6	14.20	940	0.290000
CIRS_199TI_HIRES001_VIMS	01/12/2013	51.2	124.0	14.20	1780	0.110000
CIRS_200TI_EUVFUV001_UVIS	02/01/2014	52.2	111.1	14.20	9636	1.320000
CIRS_200TI_EUVFUV002_UVIS	02/01/2014	52.2	−49.9	14.20	9117	1.320000

Table 1
(Continued)

CIRS Observation	Date	L_s (deg)	Longitude (deg W)	FWHM (cm^{-1})	FP4 N	FP4 FOV (deg)
CIRS_200TI_HIRES001_VIMS	02/01/2014	52.2	120.8	14.20	5605	0.220000
CIRS_203TI_REGMAP001_VIMS	07/04/2014	55.2	147.6	14.20	9905	0.620000
CIRS_206TI_FIRNADMAP002_PRIME	20/07/2014	58.4	−26.4	14.18	3462	0.830000
CIRS_212TI_EUVFUV001_UVIS	12/02/2015	64.7	9.9	14.18	4328	1.030000
CIRS_212TI_EUVFUV002_UVIS	13/02/2015	64.8	−156.9	14.18	3806	1.120000
CIRS_212TI_HIRES002_VIMS	12/02/2015	64.8	0.5	14.18	3552	0.030000
CIRS_213TI_FIRNADMAP002_PRIME	16/03/2015	65.7	−154.8	14.18	2790	0.770000
CIRS_215TI_FIRNADMAP002_PRIME	08/05/2015	67.4	−18.2	14.18	6183	0.510000
CIRS_215TI_HIRES001_VIMS	08/05/2015	67.4	122.5	14.18	8840	0.130000
CIRS_218TI_FIRLMBT001_PRIME	07/07/2015	69.2	−75.1	14.18	498	0.120000
CIRS_218TI_FIRNADMAP002_PRIME	07/07/2015	69.2	−139.4	14.18	6362	0.580000
CIRS_222TI_FIRNADMAP001_PRIME	28/09/2015	71.8	149.2	14.18	4345	0.520000
CIRS_230TI_EUVFUV001_UVIS	15/01/2016	75.1	23.3	14.18	7493	1.100000
CIRS_230TI_FIRNADMAP002_PRIME	16/01/2016	75.1	−143.7	14.18	6417	0.500000
CIRS_231TI_FIRNADMAP001_PRIME	31/01/2016	75.6	24.6	14.18	6052	0.550000
CIRS_232TI_FIRNADMAP002_PRIME	17/02/2016	76.1	−153.3	14.18	5390	0.570000
CIRS_234TI_EUVFUV001_UVIS	04/04/2016	77.5	16.3	14.18	9425	1.280000
CIRS_235TI_FIRNADMAP001_PRIME	06/05/2016	78.5	24.6	14.18	3131	0.670000
CIRS_236TI_FIRNADMAP001_PRIME	07/06/2016	79.4	17.8	14.18	6384	0.620000
CIRS_236TI_FIRNADMAP002_PRIME	08/06/2016	79.4	−150.6	14.18	1692	0.610000
CIRS_238TI_FIRNADMAP001_PRIME	25/07/2016	80.9	26.7	14.18	7815	0.600000
CIRS_248TI_FIRNADMAP002_PRIME	14/11/2016	84.3	−115.2	14.18	5167	0.630000
CIRS_250TI_FIRNADMAP002_PRIME	30/11/2016	84.8	−109.9	14.18	3959	0.590000
CIRS_275TI_FIRNADMAP002_PRIME	24/05/2017	90.0	−59.0	14.18	10492	1.390000
CIRS_292TI_FIRNADMAP001_PRIME	12/09/2017	93.3	−21.4	13.77	8612	1.690000

Note. The acquisition date, mean longitude, solar longitude (L_s), apodized FWHM, number of FP4 spectra (FP4 N), and FOV size are given for each observation sequence. EUVFUV are considered equivalent to FIRNADMAP observations for data analysis.

Table 1 (Figure 1). CIRS comprised two interferometer spectrometers that observed Titan in the mid- to far-IR, sensitive to the wavenumber region 10–1500 cm^{-1} across three focal planes: FP1 (10–600 cm^{-1}), FP3 (600–1100 cm^{-1}), and FP4 (1100–1500 cm^{-1}) (V. G. Kunde et al. 1996; F. M. Flasar et al. 2004). Many trace gases in Titan's atmosphere are IR-active, so CIRS spectra can provide information of the composition and temperature of Titan's atmosphere. In this study, we use IR spectra acquired by FP4, which comprises an array of 10 adjacent detectors with a full width at half-maximum (FWHM) of 0.27×0.27 mrad. CIRS had an adjustable spectral resolution, generally observing in one of three modes: high (FWHM $\sim 0.5\,cm^{-1}$), medium (FWHM $\sim 2.5\,cm^{-1}$), and low (FWHM $\sim 14.5\,cm^{-1}$) spectral resolution. Here we use "low" spectral resolution CIRS nadir observations, with an apodized spectral resolution of FWHM $\approx$ 13.5–15.5 cm^{-1} and average FWHM $= 14.25\,cm^{-1}$ (Table 1). We primarily use far-IR nadir mapping (FIRNADMAP) CIRS observation sequences, as these were taken close to Titan and typically have the highest spatial resolution of all the CIRS observation modes (F. M. Flasar et al. 2004). These were typically acquired at an approximately constant longitude, observing a large range of latitudes in one continuous slew. CIRS observations were performed on fly-bys with a typical approach distance of $\lesssim 1000 \times 10^3$ km (F. M. Flasar et al. 2004). FIRNADMAP observations were acquired at a close approach distance: approximately $(5–200) \times 10^3$ km from Titan. In addition to these, we also use far-IR nadir composition integrations (FIRNADCMP), a small number of far-IR limb temperature scans (FIRLMBT) that provided significant horizontal coverage, and some ride-along observation sequences that had a similar scanning pattern to the FIRNADMAP observations, all typically taken close-in, approximately $(20–150) \times 10^3$ km from Titan. The observations we use have a latitude field-of-view (FOV) size of $0.^{\circ}03$–$1.^{\circ}75$.

This data set has excellent spatial and temporal coverage throughout the Cassini mission (Figure 1) and the lowest noise per spectrum of any of the CIRS data. Despite this, these data are underused for atmospheric temperature and composition analysis because spectral features are subtle compared to those in higher spectral resolution nadir observations, and spectral features can often become blended. However, L. Wright et al. (2024) show that these observations can be reliably modeled using a correlated-k forward model. This data set facilitates an independent study of Titan's stratospheric tilt axis and an independent and higher spatial resolution study of Titan's polar vortices compared to, e.g., N. A. Teanby et al. (2017) and J. Sharkey et al. (2021). Measured spectra are calibrated to improve the S/N, using the procedures outlined in C. A. Nixon et al. (2014). We use the DS 4000 method, where measured spectra are compared to 4000 deep-space spectra to remove instrument self-emission. A more detailed description of the CIRS instrument and data set can be found in D. E. Jennings et al. (2017). To further improve the S/N, individual spectra were averaged in 2° latitude bins, spaced by 1° for Nyquist sampling. The high S/N of these binned spectra allows for significantly smaller latitude bin widths than in previous CIRS studies, thus preserving a high spatial resolution. Using narrow bins also means that spectra are averaged over only a small range of emission angles. At steep emission angles, the

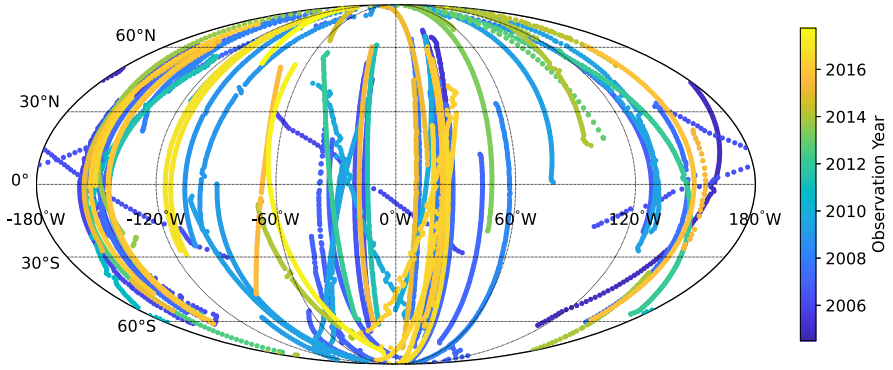

Figure 1. Observation sequences used in this study. Spectra are binned in 2° latitude bins. Points are plotted at the central latitude of the bin and at the average longitude of the bin. Color indicates the acquisition date of the observation.

radiation passes through regions of the atmosphere that may vary significantly in temperature and composition. The projected FOV size also increases closer to the limb, reducing the spatial resolution of the observation. To reduce these effects, we reject observations with emission angles greater than 70°.

3. Temperature Retrieval Method

We use the Nonlinear Optimal Estimator for MultivariatE Spectral AnalySIS (NEMESIS) radiative transfer and retrieval code (P. Irwin et al. 2008) to obtain vertical temperature profiles from the CIRS spectra. Line data are provided by databases HITRAN (I. Gordon et al. 2022) and GEISA (T. Delahaye et al. 2021). NEMESIS uses a constrained iterative nonlinear retrieval method (C. D. Rodgers 1976; J. T. Houghton et al. 1984). In the forward model, NEMESIS generates a synthetic spectrum from an a priori temperature profile using a correlated-k method (A. A. Lacis & V. Oinas 1991). In the correlated-k method, absorption coefficients are reordered by size, producing a smooth "k-distribution" that can be coarsely sampled and pretabulated in look-up k-tables. The k-tables only need to be generated once and so allow for rapid forward modeling of spectra. Absorption coefficients are calculated on a grid of 15 temperatures 70–300 K equally spaced and 20 pressures (3.1×10^{-4} mbar to 7.5×10^{3} mbar) equally spaced in log space. The instrument function associated with the CIRS instrument is a Hamming function (F. M. Flasar et al. 2004), so we compute the k-distribution using a Hamming function of width FWHM $=$ 14.25 cm^{-1}, which is the mean resolution of the observations used in this study. The k-distribution is sampled at 50 ordinates following a Gaussian quadrature scheme. L. Wright et al. (2024) show that a correlated-k method using k-tables generated with a Hamming function can reliably forward-model low spectral resolution CIRS spectra to within measurement uncertainty. A more detailed description of the forward model we use can be found in L. Wright et al. (2024).

A continuous temperature profile, in the pressure region $p = 1.4 \times 10^{3}$ mbar to 1×10^{-5} mbar, is retrieved by iterations of the forward model. With each iteration, both the difference between the measured and synthetic spectra and the departure of the retrieved profile from the a priori profile is minimized through a cost function. We fix the vertical abundance profile of methane (CH_4) assuming that it is approximately constant and well mixed throughout the stratosphere (M. Sylvestre et al. 2020). The abundance of CH_4 is set to 1.41%, as measured in situ by the Huygens atmospheric entry probe (H. B. Niemann et al. 2010). Some studies suggest that methane abundance varies significantly in the middle atmosphere (e.g., E. Lellouch et al. 2014; P. Rannou et al. 2021; P. Rannou et al. 2022; and A. E. Thelen et al. 2024); however, we fix methane abundance for consistency with previous work (e.g., N. A. Teanby et al. 2019 and J. Sharkey et al. 2021) and because, as of yet, there is no clear consensus on potential methane variability. The $CH_4\nu_4$ spectral band (1240–1360 cm^{-1}) is then fit to retrieve a continuous temperature profile, as performed by N. Teanby et al. (2006), since only CH_4 and temperature contribute to this spectral band. We test the dependence of our retrieval on the chosen fixed abundance of CH_4. We perform the same retrieval but assume a CH_4 abundance of 1.00%. Then, for a range of latitudes and times, the retrieved temperature profile assuming a 1.41% CH_4 abundance is compared to the profile retrieved assuming a 1.00% CH_4 abundance. The temperature difference is $\lesssim$2 K near 10 mbar, $\lesssim$4 K near 1 mbar, and $\lesssim$2 K near 0.1 mbar and thus does not exceed the typical retrieved temperature error, which is around 4–5 K in the stratosphere.

In an atmospheric retrieval, a forward modeling error is prescribed that limits how closely NEMESIS attempts to fit to the spectra. As a by-product of this, the solution will tend to depart less strongly from the atmospheric state of the prior iteration. We use wavenumber-dependent forward modeling errors associated with this correlated-k method, deduced by L. Wright et al. (2024), to improve the accuracy of our retrievals. We use a correlation length equal to one pressure scale height to ensure a smooth retrieved temperature profile while limiting artificial profile smoothing. We use a relatively large a priori temperature error of 5 K to prevent over-constraining the temperature. Temperature profiles in Titan's atmosphere can vary significantly with latitude and season, so we use latitude- and time-dependent a priori temperature profiles, taken from N. A. Teanby et al. (2019, their Supplementary Material S3), derived from CIRS nadir and limb data.

4. Results: Temperature Retrievals

Figure 2 shows example fits to the $CH_4\nu_4$ spectral band and the retrieved temperature profiles. The spectral fits are very good and generally within the error envelope, which is equal to the sum of the measured and forward modeling errors. The retrieved temperature profiles are typically close to the a priori profiles to within the retrieval error. However, at winter polar latitudes, the retrieved temperature profile strays from the

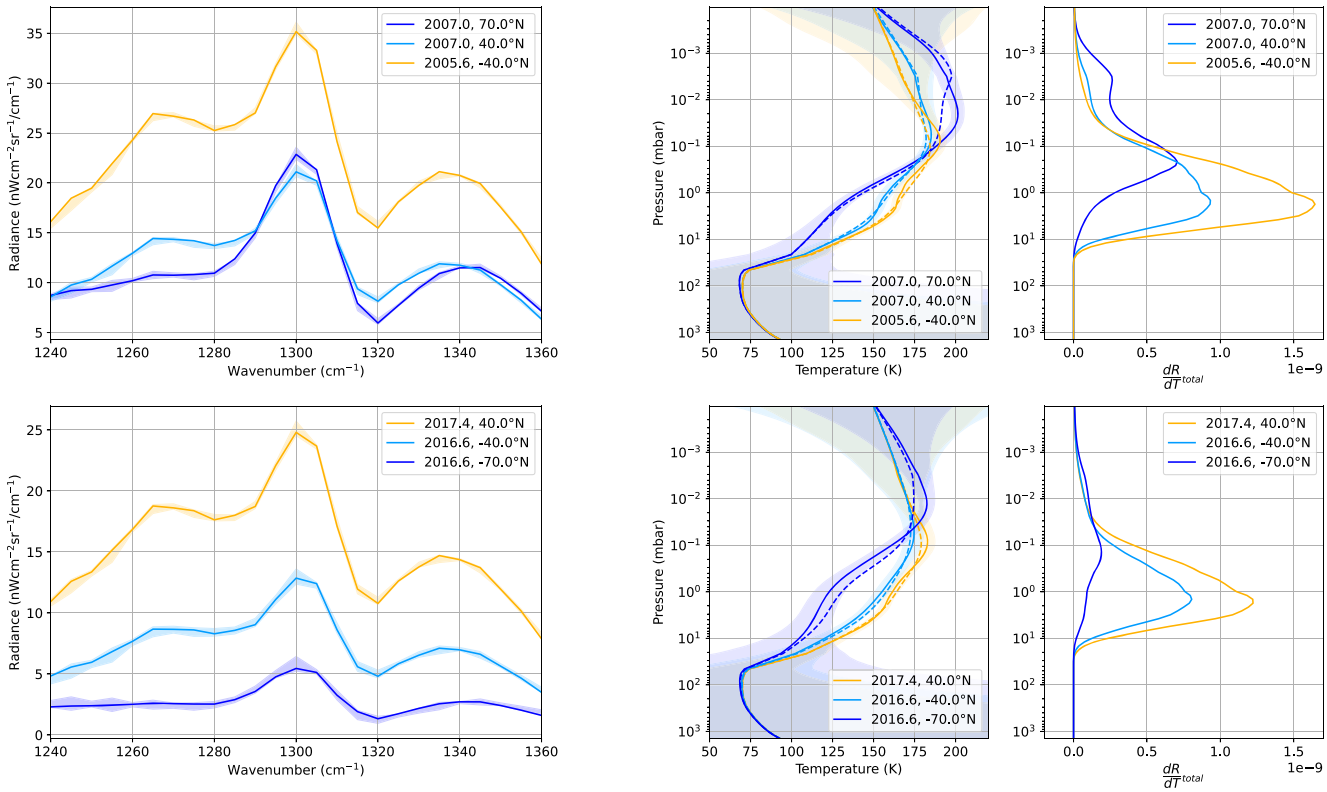

Figure 2. Example fits to averaged CIRS FP4 spectra and retrieved temperature profiles at some selected times and latitudes. Left panels show the fitted spectrum (solid lines) and measurement plus forward modeling error envelope (shaded regions). Middle panels show the retrieved atmospheric temperature profile (solid lines) and error envelope (shaded regions). The a priori temperature profiles are also plotted (dashed lines). Right panels show the corresponding contribution functions. Contribution function peaks indicate the pressure region that our nadir observations are most sensitive to. Examples are shown in Titan northern midwinter (top panels) and late northern spring (bottom panels). Winter polar latitudes are shown in dark blue, winter midlatitudes in light blue, and spring/summer midlatitudes in yellow. The contribution function shown, $\frac{dR}{dT}_{\text{total}}$, is $\frac{dR}{dT}$ summed over the fitted spectral range (1240–1360 cm^{-1}), where R is radiance and T is temperature. Observations probe higher altitudes (lower pressures) near the winter pole (dark-blue lines).

a priori profile at pressures near the hot stratopause (∼0.05–0.005 mbar). In this region, the atmosphere can be highly variable in both latitude and time. Departure from the a priori profile could also be due to our data being of a higher spatial resolution than the data used to obtain the a priori profiles (N. A. Teanby et al. 2019). The goodness of fit for the averaged spectra typically has a $\chi^2/n \approx 1$. We reject fits with $\chi^2/n > 1.5$, which compose less than 1% of fits. The unsuccessful fits are typically due to significant noise in the measured spectrum, as a result of large emission angles and large temperature gradients, and not due to issues with the retrieval. A 2D retrieval would be required to properly fit these data acquired at high emission angles (e.g., R. K. Achterberg 2023).

A contribution function is the rate of change of radiance, R, with respect to the physical quantity being retrieved—in this case, pressure-dependent temperature, $T(p)$. We determine the total contribution function, $\frac{dR}{dT}_{\text{total}} = \sum_{i=1}^{n} \frac{dR(\nu_i)}{dT(p)}$, by summing over n discrete wavenumbers, ν_i, the fitted spectral range (1240–1360 cm^{-1}; Figure 2). The contribution function peaks around 10–0.01 mbar (∼80–380 km) in the stratosphere. This indicates the altitude region that contributes most of the temperature information to our nadir observations. Near Titan's winter pole, the contribution function peak extends to lower pressures (Figure 2, dark-blue lines), indicating that the observations probe lower pressures (higher altitudes): 10–0.005 mbar (∼80–440 km), depending on the latitude and year. This is due to a large vertical thermal gradient at the winter pole as a result of trace gas enrichment. Near the winter pole, the contribution function is double peaked owing to the hot stratopause (N. A. Teanby et al. 2008).

5. Discussion

5.1. Determining the Tilt from Temperature

Temperature and composition mapping from CIRS observations shows that Titan's stratosphere is largely zonally symmetric (F. M. Flasar et al. 2005; N. Teanby et al. 2006; R. K. Achterberg et al. 2008a; N. A. Teanby et al. 2008; J. Sharkey et al. 2020). The symmetry axis of the temperature field is also the symmetry axis of the zonal wind field, through the thermal wind equation (TWE). We attempt to find the symmetry axis of the zonal temperature distribution and therefore the position of the stratospheric tilt axis. We use our measured zonal mean temperature field, which is determined on a grid of latitude, pressure, and time.

First, we apply stratospheric tilt corrections to the meridional temperature distributions using the values determined in an earlier study (J. Sharkey et al. 2020, their Table 2), with respect to the Saturn, solar, and inertial (star-fixed) reference frames (Figure 3). The tilt correction is applied by mapping latitude, longitude coordinates into a new spherical reference frame, which is tilted by angle β degrees, directed ψ degrees west of a fixed reference. In the Saturn-fixed frame, the tilt direction, ψ, is defined with respect to the Titan–Saturn vector; in the solar-fixed frame, ψ is defined with respect to the Titan–Sun vector

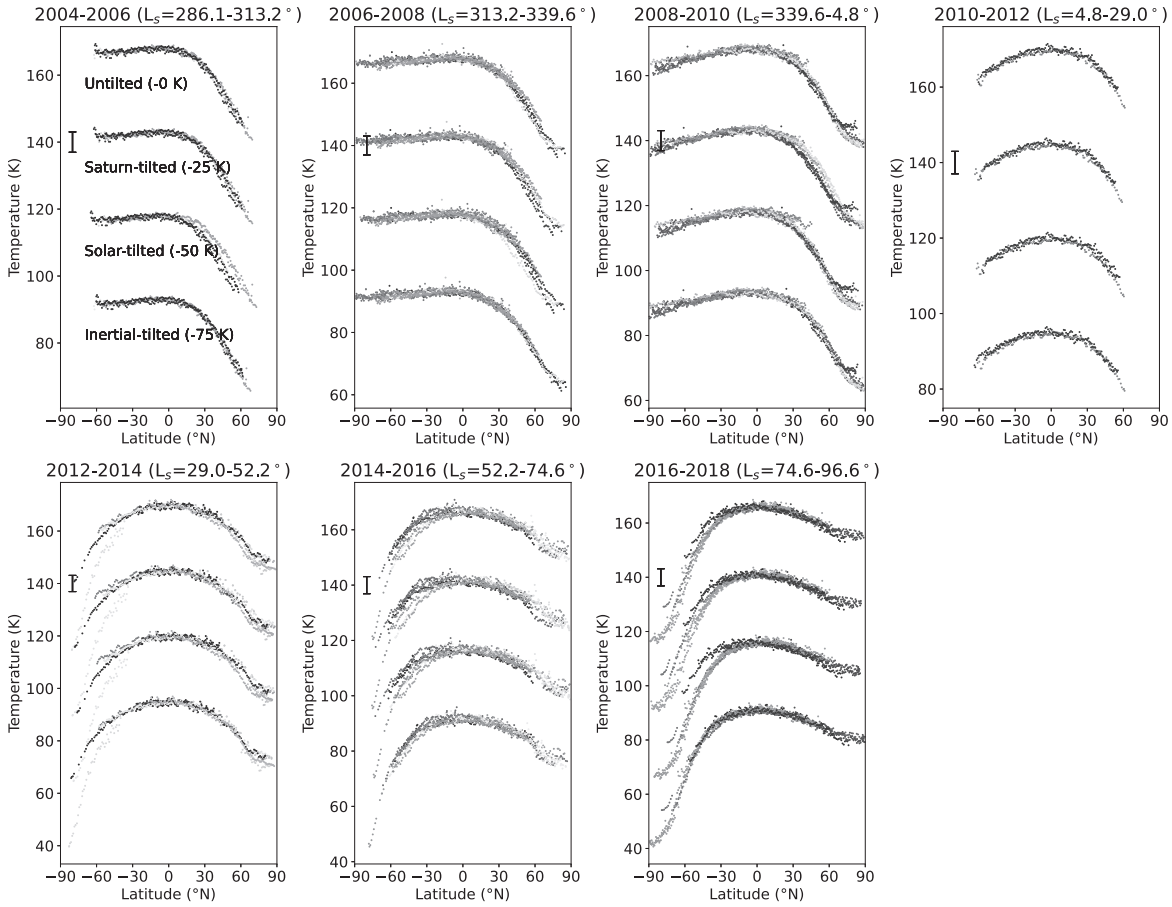

Figure 3. Latitude variation of retrieved temperature at the 1 mbar pressure level. A stratospheric tilt correction is applied in the Saturn-, solar-, and inertial-fixed reference frames using the optimal tilts determined by J. Sharkey et al. (2020, their Table 2). The points are colored according to the mean longitude of the observation sequence, to distinguish observations. A typical retrieved temperature error bar is shown for each 2 yr period. The tilt-corrected distributions generally exhibit less spread; this is particularly clear at around ±40° north (depending on the time of year), where the meridional temperature gradient is greatest.

(subsolar point); and in the inertial-fixed frame, ψ is defined with respect to the Titan–Sun vector at northern spring equinox. J. Sharkey et al. (2020) use trace gas IR emissions measured by CIRS to determine a mission-average optimal tilt in each of the three reference frames. Second, we grid search over possible tilt axes to find the optimal tilt that minimizes the spread in temperature–latitude distributions at different longitudes.

Figure 3 shows the latitude variation of temperature at the 1 mbar pressure level. Temperature distributions are compared within time bins of 2 Earth years spaced by 1 Earth year for all measured longitudes. The stratospheric temperature is not expected to vary significantly within this time frame (N. A. Teanby et al. 2019), which is equal to 0.068 Titan years, except at high latitudes ($\gtrsim$45°). Additionally, we find that the spread of temperature distributions does not appear to have a significant time dependence within each 2 yr period. Assuming zonal symmetry of the temperature field, we expect the temperature–latitude distributions observed at a range of longitudes to be approximately equal, i.e., having the smallest spread within each 2 yr period (Figure 3). The spread in the temperature–latitude distributions is therefore attributed to the offset in the stratospheric symmetry axis with respect to Titan's solid-body rotation axis. The observations we use have a good spread of subspacecraft longitudes (Figure 1) within each 2 yr period, limiting observation bias.

To determine the symmetry axis of the temperature field, we perform a grid search over tilt magnitude, β, and direction, ψ, finding the optimal tilt that minimizes the spread of temperature–latitude distributions at the 1 mbar pressure level. The spread of data within each 2 yr bin is quantified by χ^2, which sums over $i = 1, 2, \ldots, N_j$ latitudes and $j = 1, 2, \ldots, M$ observation sequences within the 2 yr bin:

$$\chi^2 = \sum_{j=1}^{M} \frac{1}{2} \sum_{i=1}^{N_j} \left(\frac{T_j(\theta_i) - T_{av}(\theta_i)}{\sigma_{ij}} \right)^2. \quad (1)$$

$T_j(\theta_i)$ is the temperature at latitude θ_i, mapped into the atmospheric tilted frame, from observation sequence j; σ_{ij} is the retrieved temperature error on $T_j(\theta_i)$; and $T_{av}(\theta_i)$ is the mean tilted temperature distribution of the 2 yr bin. The mean, $T_{av}(\theta_i)$, is determined by fitting cubic B-splines (N. A. Teanby 2007), with a knot spacing of 16°, to the tilted temperature distributions, $T_j(\theta_i)$, in the 2 yr bin. This preserves meridional structure in the temperature distributions.

In Equation (1), we include a factor of $\frac{1}{2}$ because only half of our data points are independent, as a result of the Nyquist sampling of the latitude bins. We consider temperature only within the latitude region $-45°$ north $\leqslant \theta_i \leqslant 45°$ north since stratospheric temperatures at higher latitudes are observed to vary on timescales smaller than 2 Earth years (N. A. Teanby et al. 2019). We search over a grid of tilt magnitudes, $\beta = 0°$–

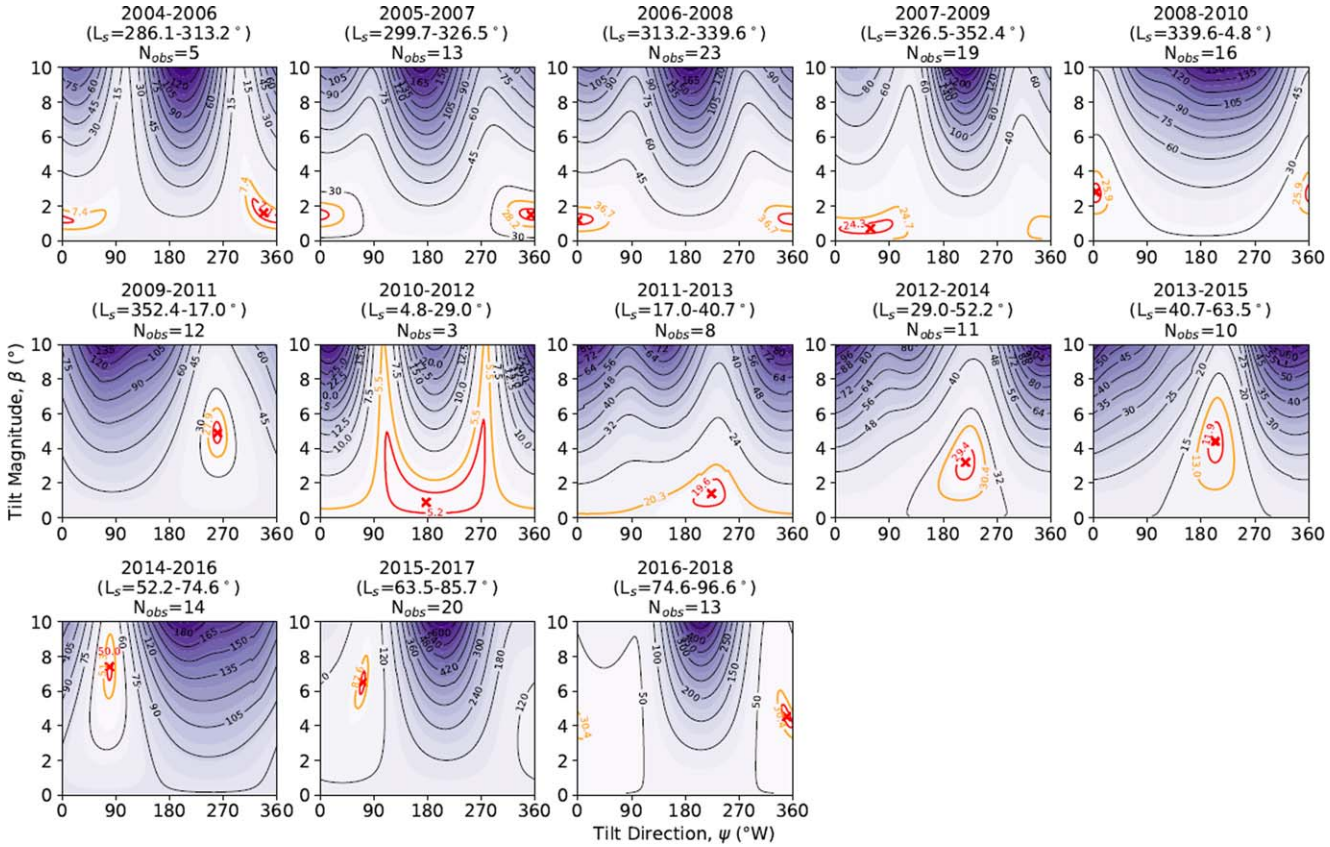

Figure 4. Grid search for optimal tilt magnitude and direction in the Saturn-fixed reference frame. χ^2 contours are shown. The location of the minimum χ^2 value is indicated with a red cross, and the 1σ (red) and 3σ (orange) confidence bounds are plotted. χ^2 quantifies the spread of temperature–latitude distributions at the 1 mbar pressure level, in each 2 yr bin. The number of observation sequences, $N_{\rm obs}$, used in each bin is given.

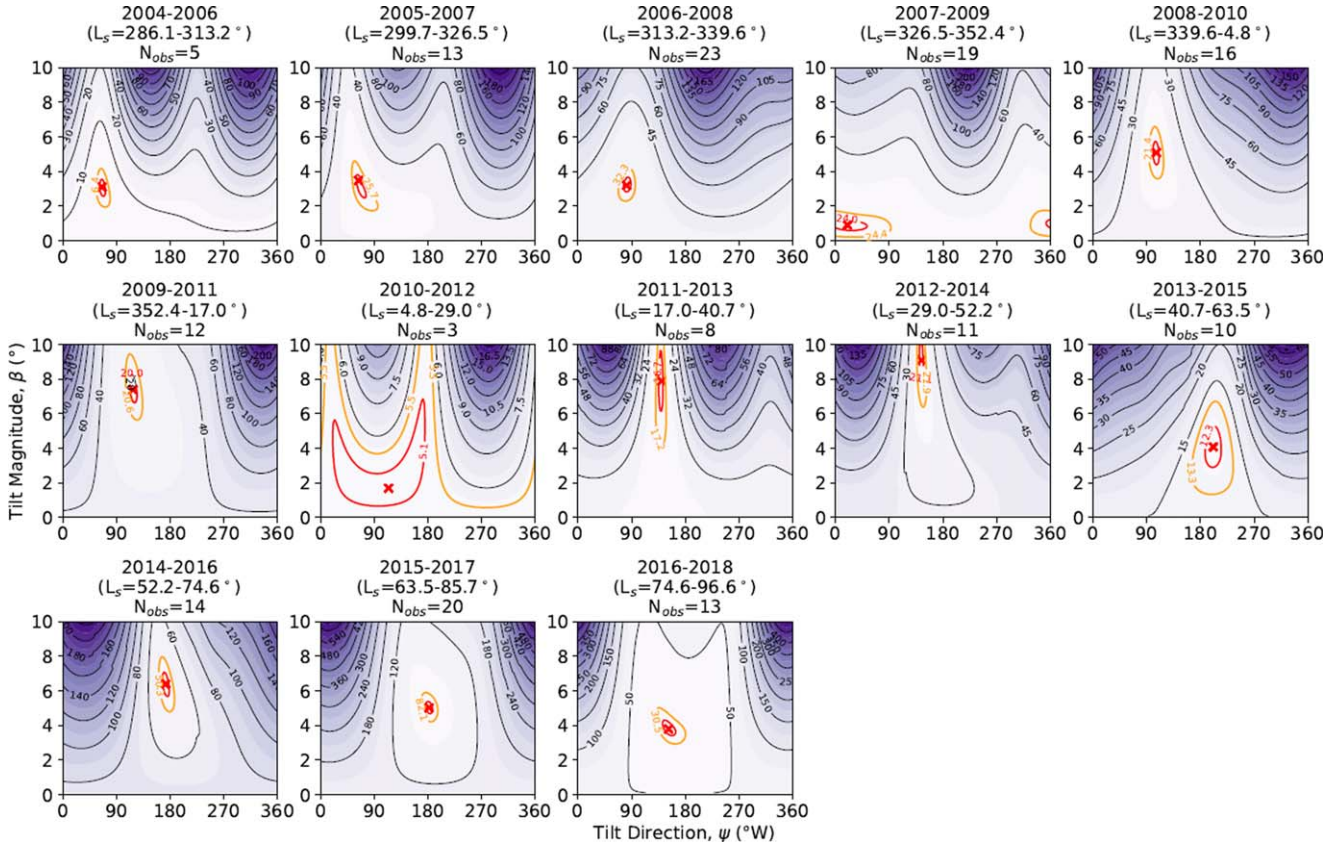

Figure 5. Same as Figure 4, but in the solar-fixed frame.

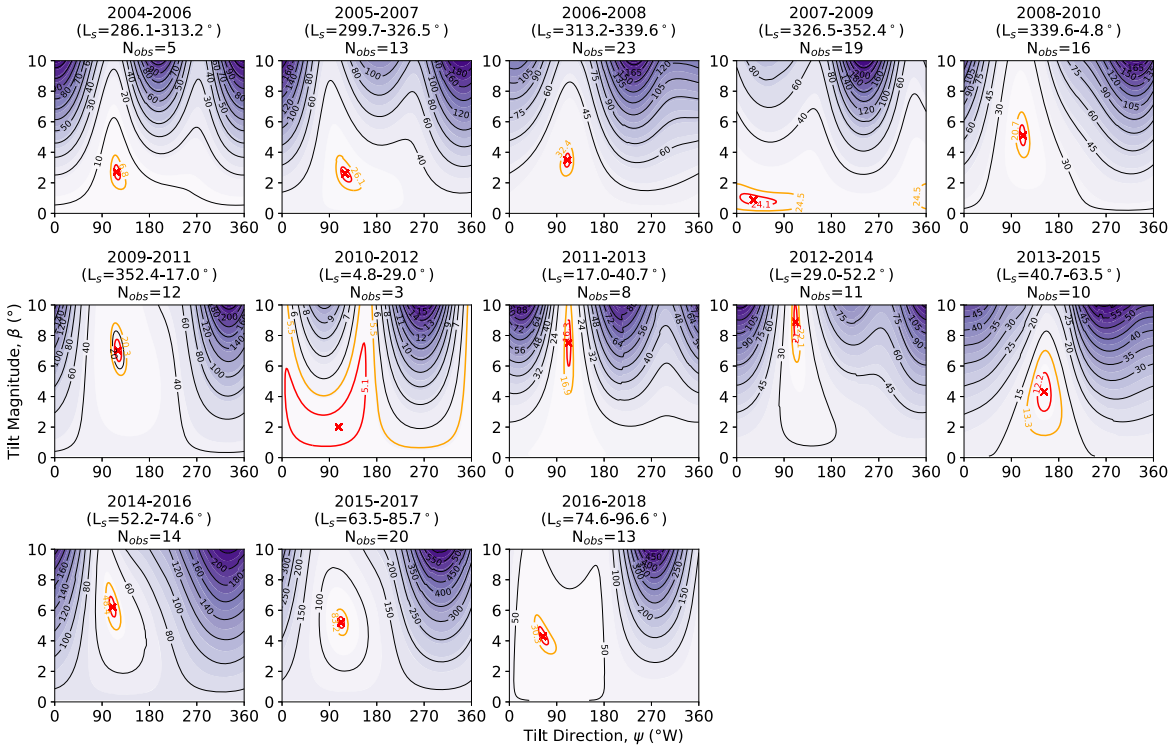

Figure 6. Same as Figure 4, but in the inertial-fixed frame.

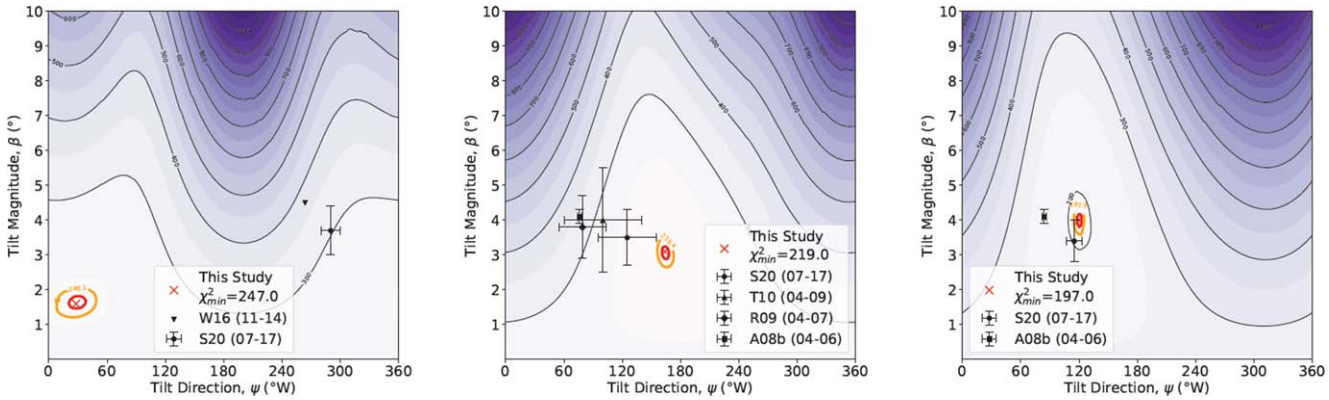

Figure 7. Grid search for optimal tilt magnitude and direction in the Saturn (left), solar (middle), and inertial-fixed (right) reference frames. χ^2 quantifies the spread of temperature–latitude distributions at the 1 mbar pressure level. χ^2 contours are shown here averaged over the full mission (2004–2017). The location of the minimum χ^2 value is indicated with a red cross, and the 1σ (red) and 3σ (orange) confidence bounds are plotted. Results from previous studies are plotted for comparison: J. Sharkey et al. (2020; S20), R. A. West et al. (2016; W16), R. K. Achterberg et al. (2008a; A08b), and M. T. Roman et al. (2009; R09).

10° spaced by 0.°1, and tilt directions, $\psi =$ 0°–360° west spaced by 2° west, fixed in the Saturn, solar, and inertial reference frames. Figures 4, 5, and 6 show the χ^2 contours for the (β, ψ) grid for each 2 yr bin in the Saturn, solar, and inertial frame, respectively. The mission-averaged χ^2 contours are plotted in Figure 7. The optimal tilt magnitudes and directions are given in Table 2.

5.2. Optimal Tilt

Optimal tilt values determined for each 2 yr bin are given in Table 2, and Figure 8 shows a time series of our determined optimal tilt values. Note that the error on the tilt for 2010–2012 is large owing to the small number of observations, of which there are 3, in that 2 yr bin. Large errors on tilt values after 2009 are likely attributed to the transitioning period post-equinox, when large-scale mixing occurs and the meridional circulation is in the process of reversing.

We find the tilt direction, ψ, to be most constant in the inertial-fixed frame. This is consistent with the findings of R. K. Achterberg et al. (2011), J. Sharkey et al. (2020), N. W. Kutsop et al. (2022), and C. Snell & D. Banfield (2024), who find the tilt direction to be largely constant in the inertial-fixed frame. The tilt direction fixed in the inertial frame gives the smallest misfit and uncertainty of the three reference frames (Figure 8). Over the full time frame of our observations (2004–2017), the mean optimal tilt is determined to be $\beta = 4.^{\circ}0 \pm 0.^{\circ}4$ directed $\psi = 120° \pm 6°$ west (3σ: ~99.7% confidence level) with respect to the subsolar point at the northern spring equinox. This is consistent with the tilt determined by J. Sharkey et al. (2020) from CIRS FP3 observations spanning the same period. In the solar-fixed

Table 2
Optimal Tilt Magnitudes (β) and Tilt Directions (ψ) Determined in This Study in the Saturn-, Solar-, and Inertial-fixed Frames

2 yr Bin	Saturn-fixed Frame		Solar-fixed Frame		Inertial-fixed Frame	
	β (deg)	ψ (deg W)	β (deg)	ψ (deg W)	β (deg)	ψ (deg W)
2004–2006	$1.6^{+2.0}_{-0.9}$	338^{+22}_{-31}	$3.1^{+1.1}_{-1.2}$	66^{+13}_{-10}	$2.7^{+1.1}_{-1.1}$	118^{+17}_{-12}
2005–2007	$1.5^{+0.8}_{-0.7}$	354^{+6}_{-40}	$3.5^{+1.1}_{-1.8}$	64^{+33}_{-11}	$2.6^{+1.2}_{-1.1}$	120^{+31}_{-18}
2006–2008	$1.2^{+0.8}_{-0.7}$	0^{+53}_{-0}	$3.2^{+1.0}_{-0.9}$	82^{+14}_{-14}	$3.5^{+1.0}_{-1.1}$	110^{+12}_{-13}
2007–2009	$0.7^{+1.3}_{-0.6}$	58^{+63}_{-58}	$0.9^{+0.8}_{-0.7}$	20^{+73}_{-20}	$0.9^{+1.0}_{-0.7}$	32^{+328}_{-32}
2008–2010	$2.8^{+1.2}_{-1.2}$	4^{+20}_{-4}	$5.1^{+1.5}_{-1.5}$	106^{+12}_{-12}	$5.1^{+1.5}_{-1.4}$	112^{+13}_{-14}
2009–2011	$4.9^{+1.4}_{-1.4}$	260^{+16}_{-16}	$7.4^{+2.1}_{-1.8}$	118^{+16}_{-13}	$7.0^{+1.8}_{-1.6}$	120^{+17}_{-14}
2010–2012	$0.9^{+9.1}_{-0.4}$	178^{+182}_{-178}	$1.7^{+8.3}_{-1.1}$	114^{+52}_{-114}	$2.0^{+8.0}_{-1.4}$	108^{+245}_{-97}
2011–2013	$1.4^{+1.7}_{-1.2}$	224^{+136}_{-44}	$7.9^{+2.1}_{-3.8}$	140^{+8}_{-10}	$7.5^{+2.5}_{-3.3}$	112^{+10}_{-8}
2012–2014	$3.2^{+2.1}_{-2.2}$	218^{+142}_{-38}	$9.1^{+0.9}_{-2.7}$	144^{+9}_{-7}	$8.9^{+1.1}_{-2.7}$	112^{+8}_{-7}
2013–2015	$4.4^{+2.5}_{-2.8}$	204^{+156}_{-24}	$4.1^{+2.6}_{-2.8}$	202^{+158}_{-22}	$4.3^{+2.7}_{-2.8}$	152^{+34}_{-33}
2014–2016	$7.4^{+1.9}_{-1.8}$	80^{+9}_{-10}	$6.4^{+1.6}_{-1.6}$	172^{+7}_{-172}	$6.2^{+1.6}_{-1.5}$	110^{+16}_{-13}
2015–2017	$6.5^{+1.6}_{-1.5}$	72^{+9}_{-13}	$5.0^{+0.9}_{-0.8}$	182^{+178}_{-2}	$5.2^{+0.9}_{-0.8}$	112^{+13}_{-12}
2016–2018	$4.5^{+1.5}_{-1.3}$	350^{+10}_{-16}	$3.8^{+1.2}_{-0.9}$	152^{+28}_{-152}	$4.3^{+1.4}_{-1.2}$	64^{+25}_{-16}
Mission Average	$1.6^{+0.4}_{-0.4}$	28^{+21}_{-21}	$3.1^{+0.4}_{-0.5}$	164^{+9}_{-8}	$4.0^{+0.4}_{-0.4}$	120^{+5}_{-6}

Notes. Errors are given as the lower/upper bounds of the 3σ (~99.7%) confidence region. Tilt directions in the solar-fixed frame given are with respect to the subsolar point (Titan–Sun vector). Tilt directions in the inertial-fixed frame are given with respect to the subsolar point at spring equinox.

frame, we determine the average tilt magnitude to be $\beta = 3.^{\circ}1 \pm 0.^{\circ}5$ and the average tilt direction to be $\psi = 164° \pm 9°$ west. These values are most consistent with those determined by J. Sharkey et al. (2020), who used CIRS observations over most of the Cassini mission (2007–2017; see Figure 7). Our determined average tilt in the solar-fixed frame is less consistent with other studies that only consider the earlier part of the mission (R. K. Achterberg et al. 2008a: 2004–2006; M. T. Roman et al. 2009: 2004–2007; N. Teanby et al. 2010: 2004–2009). Considering our time-series results, this is expected, as we observe the tilt magnitude and direction to evolve throughout the mission, in all but the inertial frame.

5.3. Tilt Axis Drift

In the solar- and inertial-fixed frames, the tilt magnitude appears to have a seasonal trend, increasing up to around 2013 and then decreasing until the end of the mission (2017). This is in agreement with R. K. Achterberg et al. (2011), who find that the tilt magnitude increases between 2005 and 2009. The tilt magnitude appears to oscillate during the Cassini mission. We fit a sinusoid to the tilt magnitude, β, in the solar- and inertial-fixed frames (Figure 8), ignoring three outliers centered at 2008, 2011, and 2014, as these have poorly constrained optimal tilt directions (Figure 8). Ignoring these outliers, the mean tilt magnitude is $\beta = 5.^{\circ}8 \pm 0.^{\circ}7$ and $\beta = 5.^{\circ}5 \pm 0.^{\circ}8$ in the solar- and inertial-fixed frames, respectively. We determine the approximate oscillation period of β to be 12.5 ± 1.5 yr in the solar-fixed frame and 13.8 ± 2.5 yr in the inertial-fixed frame—similar to half the length of a Titan year. The minimum tilt magnitude appears to occur during 2005, and the maximum appears to occur during 2013, lagging the winter solstice and vernal equinox, respectively, by around 2–3 Earth years, similar to the time it takes for the circulation to reverse after the equinox (S. Vinatier et al. 2015). This suggests that the change in tilt magnitude is perhaps related to the change in dynamical regimes.

In the inertial-fixed frame, we estimate a small eastward drift rate of $\frac{d\psi}{dt} = -1.^{\circ}1 \pm 1.^{\circ}2\,\mathrm{yr}^{-1}$. This is consistent with R. K. Achterberg et al. (2011), who find a small westward drift of $\frac{d\psi}{dt} = 1.^{\circ}1 \pm 2.^{\circ}5\,\mathrm{yr}^{-1}$. Both results are consistent with the tilt direction being fixed in the inertial frame. R. K. Achterberg et al. (2011) suggest that the tilt direction migration appears to oscillate in the inertial-fixed frame, with a period of 2.73 Earth years, although the limited time coverage of their study (5 Earth years) means that this result may not be robust, and the time resolution of our results is insufficient to resolve such oscillations.

Given that the tilt direction is approximately constant in the inertial-fixed frame, the drift rate of the tilt direction in the solar-fixed frame is expected to be equal to Titan's orbital rate, which is approximately $12°\,\mathrm{yr}^{-1}$. In the solar-fixed frame, the tilt direction appears to linearly migrate westward at a rate of $\frac{d\psi}{dt} = 9.^{\circ}3 \pm 1.^{\circ}3\,\mathrm{yr}^{-1}$, similar to Titan's orbital rate, and in agreement with R. K. Achterberg et al. (2011), who estimate a drift rate of $\frac{d\psi}{dt} = 9.^{\circ}1 \pm 2.^{\circ}5\,\mathrm{yr}^{-1}$ in the solar-fixed frame. Our drift rate is also broadly consistent with C. Snell & D. Banfield (2024), who estimate a westward migration of $\cdot\,\mathrm{yr}^{-1}$ from Cassini/ISS observations of Titan's north–south haze asymmetry boundary. The optimal tilt directions we determine are generally in good agreement with those determined by C. Snell & D. Banfield (2024) (Figure 8, middle right panel, green points). Note that there is a large spread of points after around 2014 in the results of C. Snell & D. Banfield (2024). These typically have large uncertainties due to "difficult viewing geometries" and a "fuzzier boundary toward the end of the mission" (C. Snell & D. Banfield 2024). N. W. Kutsop et al. (2022) also predict a westward drift of the tilt direction in the solar frame but estimate $\frac{d\psi}{dt} = 2.^{\circ}6 \pm 2.^{\circ}8\,\mathrm{yr}^{-1}$ and $\frac{d\psi}{dt} = 47.^{\circ}0 \pm 12.^{\circ}1\,\mathrm{yr}^{-1}$ from Cassini/VIMS observations of the equatorial and northern haze annuli, respectively. In the inertial-fixed frame, the tilt direction appears largely constant, potentially with a very slow eastward migration.

Currently, the stratospheric tilt is not reproduced in most Titan GCMs. The horizontal resolution of present GCMs is ~5° (C. E. Newman et al. 2011; N. A. Lombardo &

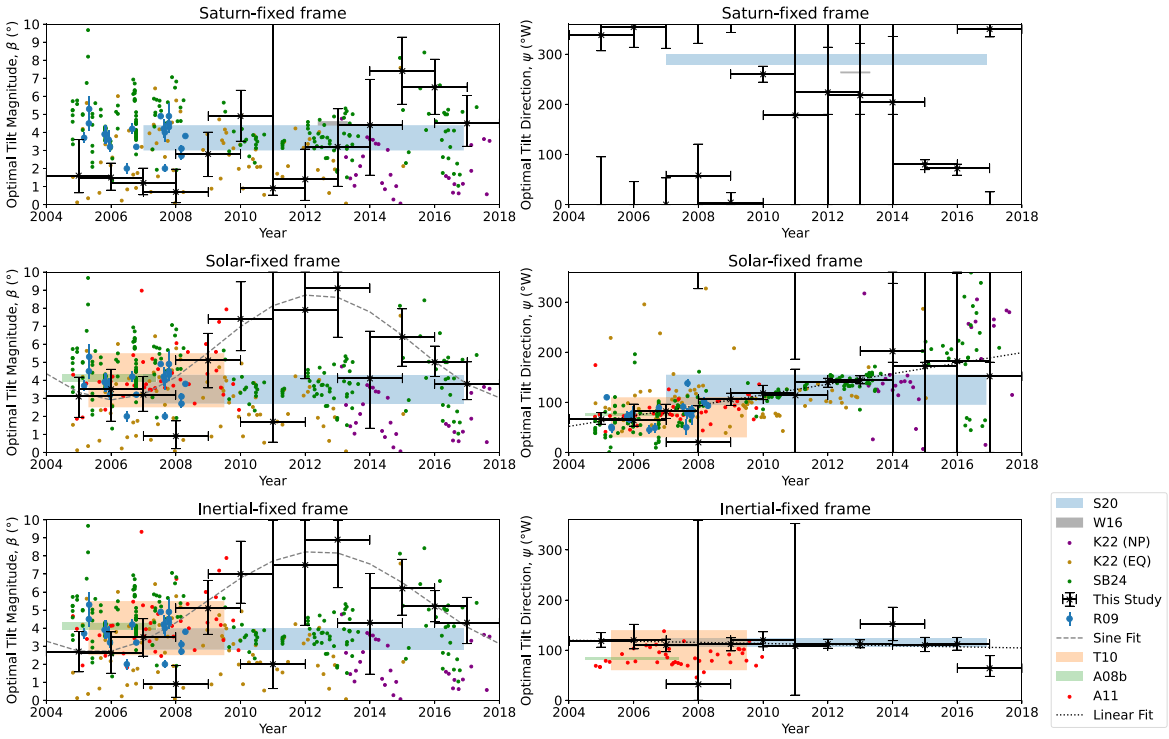

Figure 8. Time series of the optimal tilt magnitude (left panels) and direction (right panels) for each 2 yr bin. The optimal tilt is that which minimizes the spread of temperature–latitude distributions within each 2 yr bin. Results from previous studies are plotted for comparison, although these vary slightly in altitude: J. Sharkey et al. (2020; S20), ∼1 mbar (∼190 km); R. A. West et al. (2016; W16), ∼0.08 mbar (∼300 km); R. K. Achterberg et al. (2008a; A08b), ∼1 mbar (∼190 km); N. W. Kutsop et al. (2022; K22 using north polar haze annulus (NP) and equatorial haze annulus (EQ)), at pressures $\lesssim$8 mbar (∼100 km); R. K. Achterberg et al. (2011; A11), ∼1 mbar (∼190 km); M. T. Roman et al. (2009; R09), at ∼15 mbar (∼80 km); C. Snell & D. Banfield (2024; SB24), ∼70–0.6 mbar (∼50–200 km). A linear fit is plotted for the tilt direction in the solar- and inertial-fixed frames (black dotted lines), and a sinusoid is fit to the tilt magnitude in the solar- and inertial-fixed frames (gray dotted line), ignoring three outliers.

J. M. Lora 2023b), which is likely too low to resolve a tilt of around $\beta = 4°$. However, a stratospheric tilt is reproduced in one GCM (T. Tokano 2010). T. Tokano (2010) finds the atmospheric angular momentum vector, i.e., the atmospheric rotation axis with respect to the solid-body rotation axis, to have a westward precession due to thermal tides inducing wavenumber-1 oscillations in the zonal and meridional wind field. However, we determine the tilt direction to be fixed in the inertial frame, suggesting that the tilt is not directly caused by solar-induced thermal tides (as also found by, e.g., N. W. Kutsop et al. 2022). T. Tokano (2010) determines the tilt magnitude to have a seasonal dependence, decreasing toward the center of the mission, with a minimum at $L_s \approx 50°$ (2014). We observe the opposite trend in the solar- and inertial-fixed frames, although the uncertainties on our tilt magnitude values are significant.

The mechanism behind the tilt and the reason for the direction being fixed in inertial space remain an open question. The direction of the tilt axis being constant in the inertial frame means that it has a fixed direction in inertial space (Figure 9), which suggests that the atmospheric rotation axis acts as a gyroscope, stabilizing itself in a fixed direction. If we think of Titan's massive, superrotating stratosphere as being essentially decoupled from the lower atmosphere and solid body, as suggested by M. K. Bird et al. (2005), we might expect this high angular momentum stratosphere to require a large external torque to change the tilt direction in inertial space. Perhaps the stratospheric rotation axis was disturbed from its axisymmetric state in the past and the tilt axis has since remained in a fixed direction in inertial space. The cause of this disturbance is unknown, but contenders could be an impact event, long-term orbital precession and related climatic changes, and the asymmetric northern lake distribution. T. Tokano (2010) showed that solar tides also could be an important mechanism. A future, higher-resolution Titan GCM study may help determine the mechanism driving the stratospheric tilt.

5.4. Temperature Field, Zonal Winds, and Potential Vorticity

Here we consider the zonal mean temperature, wind, and PV in Titan's stratosphere and compare our observations with a model and with previous studies. The observations used in this study have a much higher spatial resolution than in previous work, providing an improved perspective on seasonal changes in Titan's stratosphere throughout the Cassini mission.

The zonal wind shear in an atmosphere is related to the meridional temperature gradient through the TWE. We use the TWE to determine the zonal mean wind field in Titan's stratosphere from the zonal mean temperature field. Zonal wind speeds in Titan's stratosphere have been determined previously using the TWE and CIRS nadir and limb observations by F. M. Flasar et al. (2005), R. K. Achterberg et al. (2008a), R. K. Achterberg et al. (2011), N. A. Teanby et al. (2008), S. Vinatier et al. (2020), and J. Sharkey et al. (2021). The observations we use in this study offer a higher meridional resolution (2°) than in previous studies (e.g., ∼7.°5, J. Sharkey et al. 2021; ∼13.°5, R. K. Achterberg et al. 2011).

PV, q, is a key quantity in diagnosing the dynamics of a rotating fluid, such as a planetary atmosphere, as it is materially conserved in adiabatic, frictionless flows. We use the TWE to estimate wind speeds from the zonal mean temperature. We

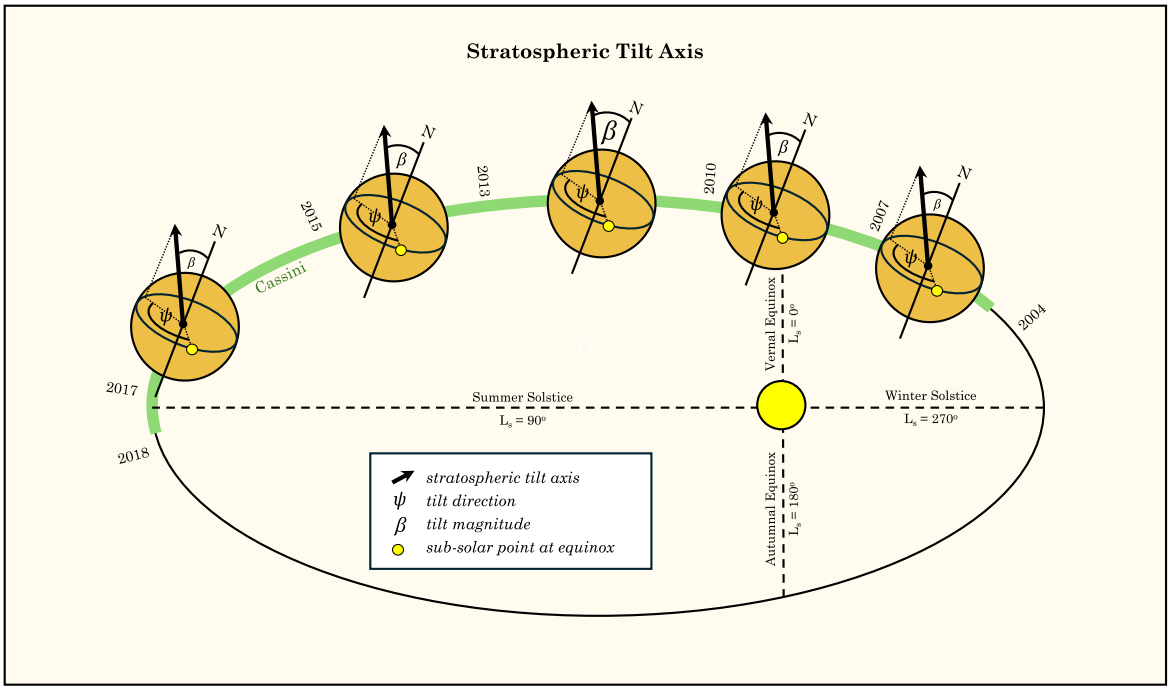

Figure 9. Schematic showing the direction of Titan's stratospheric tilt axis determined in this work, throughout the Cassini mission. Titan is shown at some example times in its orbit, during the time span of the Cassini mission (2004–2017). The tilt direction is determined to be approximately constant in the inertial reference frame, that is, fixed with respect to the Titan–Sun vector at the northern spring (vernal) equinox ($L_s = 0°$). The approximate size of the tilt magnitude, β, is indicated by font size.

then determine the seasonal variation of PV from the zonal mean temperature and wind field.

5.4.1. High Meridional Resolution Temperature Field

Figure 10 shows zonal cross sections of retrieved temperature, averaged over each Earth year during the Cassini mission. This is the highest meridional resolution temperature field observed in this pressure region to date. The effects of the stratospheric tilt have been removed by mapping the temperature field into the tilted frame, such that given latitudes are in the atmospheric frame rather than Titan's solid-body frame. We use the mission-average optimal tilt axis determined in Section 5.1 in the inertial-fixed frame (tilt $\beta = 4.^{\circ}0$, directed $\psi = 120°$ west of the subsolar point at northern spring equinox). The uncertainty on the retrieved temperature is typically 5 K at pressures greater than 0.1 mbar level, around 5–10 K in the 0.1–0.01 mbar region, and around 10–20 K at pressures less than 0.01 mbar, which approaches the pressure limits probed by the CIRS nadir observations used in this study (Figure 2).

Our retrieved temperature structures are in broad agreement with those found by limb (R. K. Achterberg et al. 2008a, 2011; S. Vinatier et al. 2015, 2020; N. A. Teanby et al. 2017, 2019) and nadir observations (J. Sharkey et al. 2021; R. K. Achterberg 2023). Early in the mission, in mid- to late northern winter, we observe a high and hot stratopause at the north pole. An elevated winter polar stratopause is observed in previous studies (R. K. Achterberg et al. 2008a, 2011; S. Vinatier et al. 2015; R. K. Achterberg 2023) and in a Titan GCM (N. A. Lombardo & J. M. Lora 2023b). Pre-equinox (2004–2009, $L_s < 360°$), we observe the north polar stratopause to be approximately 205 K and located at around 0.01 mbar. The stratopause at lower latitudes, south of ∼60° north, is around 15 K cooler and about a decade deeper in pressure, in agreement with R. K. Achterberg et al. (2008a).

The stratopause is observed to be hot at the winter pole, most likely due to adiabatic heating of the descending branch of the meridional circulation cell (N. A. Teanby et al. 2017). Lower in the stratosphere, north polar temperatures are much colder than the stratopause, with temperatures reaching almost as low as 115 K at the 5 mbar level. These temperatures are lower than the TAM temperatures (∼140 K) but similar to the ∼120 K temperatures observed by P. Rannou et al. (2004) and S. Lebonnois et al. (2012), who include microphysics and photochemistry in their models. These extremely cold temperatures can be explained by the presence of trace molecules, acting as long-wave radiative coolers, which have been observed to be enriched at the winter pole (N. A. Teanby et al. 2017, 2019). Trace gases produced in the upper atmosphere descend with the circulation at the winter pole into the polar vortex, which acts as a mixing barrier, effectively trapping the trace gases at the winter pole (N. A. Teanby et al. 2008).

In the 2 yr leading up to the equinox (Figure 10, panels 2008 and 2009), the north polar stratopause cools slightly by ∼15 K, consistent with values found by R. K. Achterberg et al. (2011), S. Vinatier et al. (2015), N. A. Teanby et al. (2017), and R. K. Achterberg (2023), but remains warm and elevated compared to the stratopause at lower latitudes. This is most likely due to weakening of the meridional circulation cell (R. K. Achterberg et al. 2011), where the velocity of the descending branch decreases, leading to reduced adiabatic heating at the north pole. We observe a global decrease in stratospheric temperatures from 2006 to 2013, consistent with the reduced solar flux received by Titan during this period, due to Saturn's orbital eccentricity (S. Vinatier et al. 2015).

Post-equinox (after 2009 August, $L_s > 0°$), the north polar stratopause is observed to gradually cool by ∼20 K and

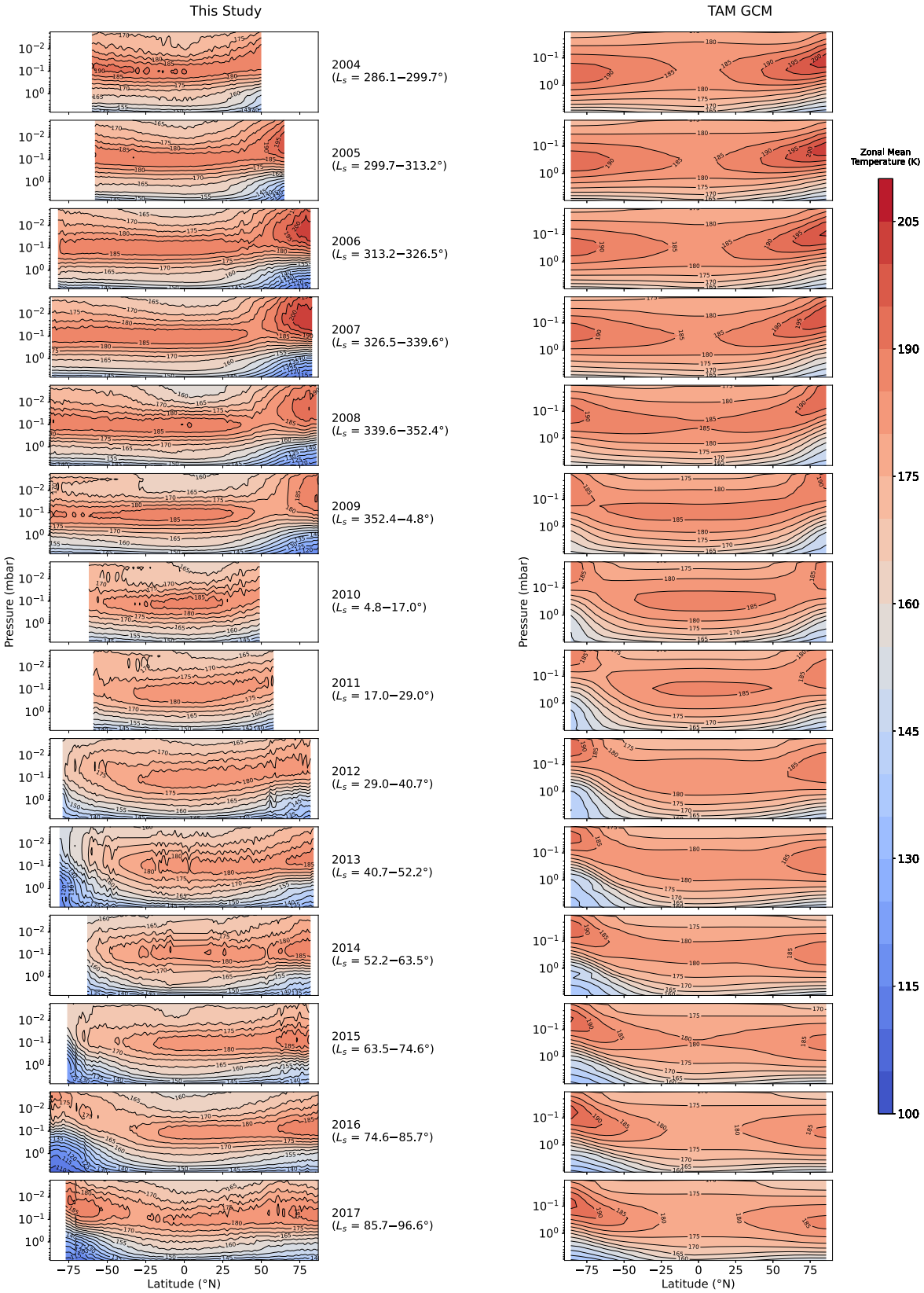

Figure 10. Zonal mean temperature field in the stratosphere, averaged in 1-Earth-year bins. Left: observed temperature field in this study. Right: zonal mean temperature simulated by TAM (N. A. Lombardo & J. M. Lora 2023b, 2023a). The mean optimal stratospheric tilt found in Section 5.1, fixed in the inertial frame, has been applied to the observed temperature field (left). The TAM data are plotted over a pressure range corresponding to the vertical extent of the stratosphere and mesosphere probed by the CIRS data.

descends to the same level as the lower-latitude stratopause (∼0.01 mbar). However, the north polar stratopause remains around 10 K warmer than lower latitudes throughout the remainder of the mission, consistent with CIRS limb observations (S. Vinatier et al. 2015, 2020; R. K. Achterberg 2023). At the south pole, we observe an elevated stratopause from at least 2012 ($L_s \approx 30°$), which cools during 2012–2014, before warming again in early 2016 ($L_s \approx 75°$). This behavior is consistent with that found by R. K. Achterberg (2023). From at least 2012, the lower south polar stratosphere (pressures greater than ∼0.1 mbar) rapidly cools and continues to do so until the end of the mission, with temperatures dropping to approximately 120 K at pressures greater than 1 mbar. Rapid cooling of the lower stratosphere is consistent with other nadir observations (N. A. Teanby et al. 2017; J. Sharkey et al. 2021) and with limb observations (S. Vinatier et al. 2020; R. K. Achterberg 2023) and is similar to what we observe in the lower north polar stratosphere during late northern winter. This unexpected cooling is, again, likely caused by long-wave-emitting trace species (N. A. Teanby et al. 2017), which become enriched at the south pole after the global circulation reversal.

By around mid-2016 ($L_s \approx 80°$), a high and hot stratopause has formed over the south pole, at around 0.002 mbar, consistent with N. A. Teanby et al. (2017), J. Sharkey et al. (2021), and S. Vinatier et al. (2020). This is higher than the hot stratopause observed in the north during northern winter, but Cassini observations are not seasonally symmetric, as the mission did not capture the beginning of northern winter. The hot south polar stratopause then warms and descends to ∼0.01 mbar, extending away from the pole (Figure 10, panel 2017)—still a factor of 10 deeper in the atmosphere than the stratopause at ∼0.1 mbar, consistent with limb observations (S. Vinatier et al. 2020). This is most likely due to strengthening of the descending branch of the meridional circulation, leading to increased adiabatic heating at high southern latitudes (N. A. Teanby et al. 2017).

Figure 10 shows our retrieved zonal mean temperature and also the zonal mean temperature field produced by TAM (N. A. Lombardo & J. M. Lora 2023b, 2023a). TAM is a three-dimensional GCM that has been used extensively to study Titan's lower atmosphere and climate. Recently, TAM has been updated to improve the vertical extent and resolution of the model, as well as to include the radiative impacts of seasonally varying radiative species. The three-dimensional nature of TAM allows for the direct simulation of three-dimensional eddies, which have been shown to be crucial in the transportation of momentum through the middle atmosphere. The simulations presented here are based on the configuration of the model presented in N. A. Lombardo & J. M. Lora (2023b) and include an approximate 5° meridional resolution and 50 atmospheric layers distributed from the surface to an altitude of approximately 500 km (10^{-2} Pa; N. T. Lewis et al. 2023; J. M. Lora et al. 2015). TAM temperatures are shown for the period of Titan's seasonal cycle covered by our observations and have been averaged over the same Earth-year bins to allow for a direct comparison.

The stratopause in the TAM temperature field is roughly a factor of 5 deeper in pressure compared to our observed temperature in all time bins (Figure 10). A ubiquitous challenge in comparing observations of Titan's middle atmosphere with GCM simulations is accounting for the decreasing strength of the gravitational acceleration with altitude. The dynamical cores of many Titan GCMs assume a uniform gravity, which, while accurate for Earth's very thin atmosphere, introduces discrepancies at the high altitudes of Titan's middle atmosphere. This leads to the effective altitude of pressure levels in Titan GCMs being lower than in reality. Along the same lines, the high strength of Titan's zonal winds leads to an atmospheric equatorial bulge, which is not included in most Titan GCMs (N. A. Lombardo & J. M. Lora 2023a). For the most robust insight into Titan's dynamics, it is best to compare observations and simulations not by direct altitude or pressure comparisons but by the structure of the atmospheric layers themselves, e.g., compare the temperature and winds of the observed stratosphere with those of the simulated stratosphere, regardless of exact altitude. We plot the TAM temperature field in Figure 10 over a reduced pressure range to facilitate a more realistic comparison to our observations. The evolution of our observed mean zonal temperature is broadly consistent with the average zonal temperatures produced by TAM.

In northern winter, we observe a hot, elevated stratopause at the north pole. A similarly hot stratopause (∼205 K) is obtained in TAM (N. A. Lombardo & J. M. Lora 2023b, 2023a) temperature cross sections, but the hot spot is much more confined to polar latitudes compared to the TAM temperature (Figure 10). The TAM temperature also exhibits a hot, although not elevated, stratopause (∼195 K) at the south summer pole that is much less pronounced. During mid- to late northern winter, the TAM temperature field is almost symmetric about the equator, whereas our observations show a clear asymmetry, with an elevated hot spot over the north pole that is constrained to high latitudes, but we do not observe the same feature at the summer south pole.

In the TAM temperature field, the south polar hot spot persists, becoming hotter and more elevated post-equinox (after 2009, $L_s > 0°$), suggesting that the south polar vortex develops more quickly post-equinox in the TAM simulation compared to observations. We only observe a south polar hot spot in 2016 ($L_s \approx 75°$–$86°$). During 2012–2015, and most noticeably in 2013 ($L_s \approx 40°$–$52°$), we observe a cold spot at the south pole, around 0.1–0.01 mbar, which is not reproduced with the TAM. Instead, TAM produces a hot spot at the south pole immediately post-equinox (Figure 10, right 2009 panel). This may be due to the absence of highly enriched trace gas coolers in the model, as suggested by N. A. Teanby et al. (2017). Broadly, the observed and simulated temperature fields are in good agreement, especially during times when the atmosphere is more stable and the polar vortex is established, i.e., 2004–2009 and 2016–2018, although the observed south polar stratosphere is much colder than the simulation (Figure 10). The observed and TAM temperatures exhibit some common features, including a hot, elevated stratopause and a cold, lower stratosphere at the winter pole. At the northern winter pole (2005–2010, $L_s < 0°$), we observe temperatures around 110–150 K at pressures greater than ∼1 mbar, whereas the TAM produces temperatures around 160–180 K. Similarly, post-equinox, the cold lower-stratospheric temperatures at the south pole are around 110–120 K in our observations, compared to around 140–150 K in TAM. During the transitional period post-equinox, the observed and simulated temperatures are somewhat similar, but perhaps with an offset in the transition timing.

5.4.2. Zonal Winds

Titan's atmosphere is generally in cyclostrophic balance, such that the meridional pressure gradient is balanced with the total horizontal component of the centrifugal force. For such an atmosphere, the vertical gradient of the zonal wind is related to the meridional temperature gradient through the TWE. This is expected to hold for Titan (F. M. Flasar et al. 2005). The TWE can be written as (F. M. Flasar et al. 2005)

$$\frac{\partial}{\partial z_{||}}\left(2\Omega u + \frac{u^2}{r\cos\phi}\right) = -\frac{g}{T}\frac{1}{r}\frac{\partial T}{\partial \phi}\bigg|_p, \tag{2}$$

where Ω is the solid-body rotation rate of Titan, u is the (eastward) zonal wind velocity, ϕ is the latitude, g is the gravitational acceleration, T is the temperature, p is the pressure, r is the radial polar coordinate (radius of Titan + altitude: $r = R_T + h$), and $z_{||}$ is the axis parallel to Titan's atmospheric rotation axis. To calculate zonal wind speed, we integrate the TWE over cylinders concentric to Titan's rotation axis (along the $z_{||}$ axis; see, e.g., F. M. Flasar et al. 2005, supplementary material for integration). Consequently, the zonal wind speed is unconstrained by the TWE at low latitudes, although P. S. Marcus et al. (2019) show that an equatorial TWE can be formulated for some planetary atmospheres.

We use a finite-difference method to approximate the differential in Equation (2):

$$\left(\frac{\partial T}{\partial \phi}\bigg|_p\right)_{ij} = \frac{1}{\phi_{i+1} - \phi_{i-1}}[T_{i+1,j} - T_{i-1,j}], \tag{3}$$

for the ith latitude and jth pressure level in Titan's stratosphere, and $T_{ij} = T(p_j, \phi_i)$. Calculating the zonal wind speed field requires a boundary condition. We apply the boundary condition setting the zonal wind speed at 10 mbar as 4 times Titan's solid-body rotation rate ($u(p = 10\ \text{mbar}) = 4\Omega$), as used in R. K. Achterberg et al. (2008a), which is consistent with the Doppler wind experiment on board the Huygens descent probe (M. K. Bird et al. 2005; W. M. Folkner et al. 2006).

Since the zonal wind is dependent on the temperature meridional gradient, the temperature field must be smoothed before the TWE is applied, to limit the amplification of noise. We smooth the Earth-year average temperature field by fitting cubic B-splines (N. A. Teanby 2007) with a knot spacing of 10° and then calculate the mean zonal wind. This local fitting procedure preserves local temperature gradients better than the smoothing applied in previous studies (R. K. Achterberg et al. 2011; J. Sharkey et al. 2021). This, in addition to the higher meridional resolution of the underlying temperature field, preserves finer features in the zonal wind field. The resulting resolution of our zonal wind field is approximately 15°. The low spectral resolution nadir CIRS observations used in this study probe a narrower vertical range, and hence achieve a smoother vertical temperature gradient, than the higher spectral resolution nadir observations used by J. Sharkey et al. (2021). Additionally, our observations have a more consistent coverage of latitudes: while the S/N in J. Sharkey et al. (2021) becomes poor near the pole, due to their binning procedure, our S/N is more consistent over all latitudes. Thus, at high latitudes, we achieve a better S/N, and hence a more robust zonal wind field, than J. Sharkey et al. (2021). Thus, despite the effects of smoothing producing a wind field with a comparable meridional resolution, our observations can better preserve meridional structure in the zonal wind field.

Figure 11 shows the zonal mean wind field velocities derived from the mean zonal temperature. Determining zonal wind speed, u, from the TWE requires solving a quadratic in u, for which the discriminant can sometimes be negative, most typically due to noisy data. Consequently, the zonal wind speed cannot be calculated in some regions, typically where the meridional temperature gradient is small, in addition to being unconstrained near the equator (Figure 11). The unconstrained equatorial region has been determined previously through stellar occultations in northern midwinter (B. Sicardy et al. 2006) and with ground-based millimeter-wave observations (E. Lellouch et al. 2019; M. A. Cordiner et al. 2020; S. Light et al. 2024). We estimate the uncertainty in the zonal wind using the retrieved temperature error (outlined in the Appendix). The uncertainty in the zonal wind field is typically 2–15 m s^{-1}. In Figure 11, the regions where the wind speed error exceeds the contour interval (>10 m s^{-1}) are not plotted.

Figure 11 also shows the zonal mean wind speeds produced by TAM (N. A. Lombardo & J. M. Lora 2023b, 2023a). Note that the TAM wind field is plotted over a reduced pressure range to compensate for Titan GCMs having a slightly depressed atmosphere compared to observations. The zonal winds have been averaged over the same Earth-year bins as our observations to allow for a direct comparison. The structure and evolution of our mean zonal wind field are overall in good agreement with previous studies using CIRS limb (S. Vinatier et al. 2020) and CIRS nadir (J. Sharkey et al. 2021) observations. However, our improved spatial resolution allows finer structure to be resolved. The observed wind field is also in good agreement with the TAM wind (N. A. Lombardo & J. M. Lora 2023b, 2023a), although TAM produces overall lower wind speeds.

The TAM winds also exhibit a second, weaker zonal wind maximum at ∼0.002 mbar (outside the range plotted in Figure 11), which we do not observe, perhaps due to the vertical shift that occurs in the GCM results and the limited sensitivity at these pressures. We observe the southern hemisphere circumpolar jet to reach higher wind speeds than the northern jet, in agreement with S. Vinatier et al. (2020) and J. Sharkey et al. (2021). Peak wind speeds are observed to be around 210 m s^{-1} in the north and 230 m s^{-1} in the south, with an uncertainty within 10 m s^{-1}. These values are comparable to the peak wind speeds observed by J. Sharkey et al. (2021; close to 200 m s^{-1} in the north and 220 m s^{-1} in the south) and R. K. Achterberg (2023; close to 200 m s^{-1} in the north and 250 m s^{-1} in the south). S. Vinatier et al. (2020) observe wind speeds of 240–280 m s^{-1} in the south. Our observed winds are slightly slower than those of J. Sharkey et al. (2021), likely due to the higher meridional resolution of our observations, which better preserve the horizontal temperature gradient. On the other hand, our wind speeds are slightly slower than those observed by S. Vinatier et al. (2020), perhaps due to the viewing geometry of our observations. Nadir observations give a smoother temperature profile, and hence less extreme winds, whereas limb observations, used by S. Vinatier et al. (2020), better resolve vertical temperature structure and hence better preserve high wind speeds. Our observed wind speeds are significantly faster than those simulated by TAM (Figure 11), which produces wind speeds around 130 m s^{-1} in the north and

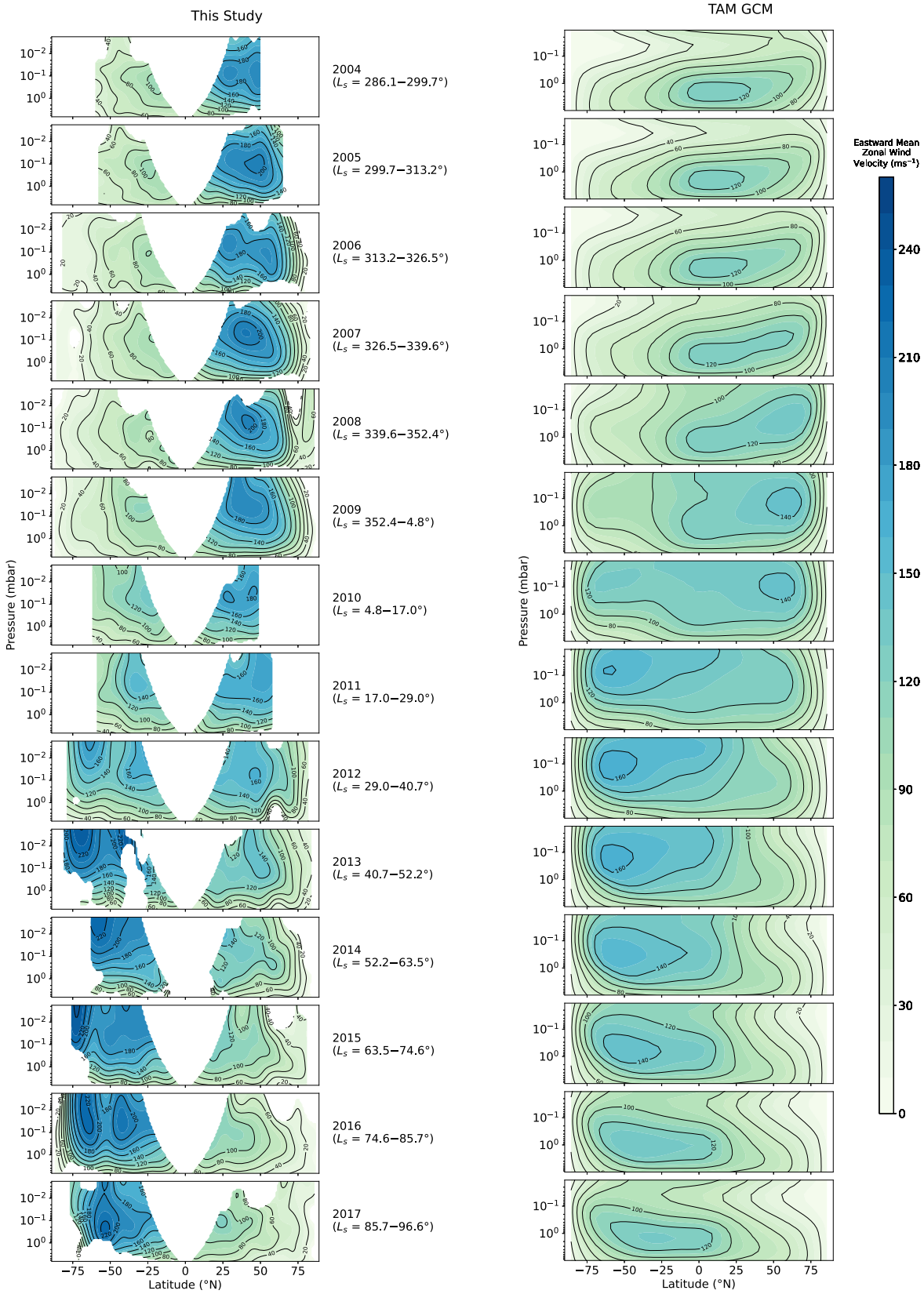

Figure 11. Eastward zonal mean wind speed, u. Left: wind speeds calculated using the TWE and the observed mean zonal temperature field. Right: wind speeds simulated using TAM (N. A. Lombardo & J. M. Lora 2023b, 2023a). The wind field has been averaged in 1-Earth-year bins. Wind speeds are calculated from the temperature field smoothed with cubic B-splines with a knot spacing of 10° (left) and assuming that the zonal wind speed at 10 mbar is 4 times Titan's solid-body rotation rate. The TWE is unconstrained near the equator, and the zonal wind speed cannot be determined in some regions, typically due to significant noise in the data or lack of observation coverage. Regions where the wind speed error exceeds the contour interval (>10 m s^{-1}) have not been plotted. The TAM data are plotted over a pressure range corresponding to the vertical extent of the stratosphere and mesosphere probed by the CIRS data.

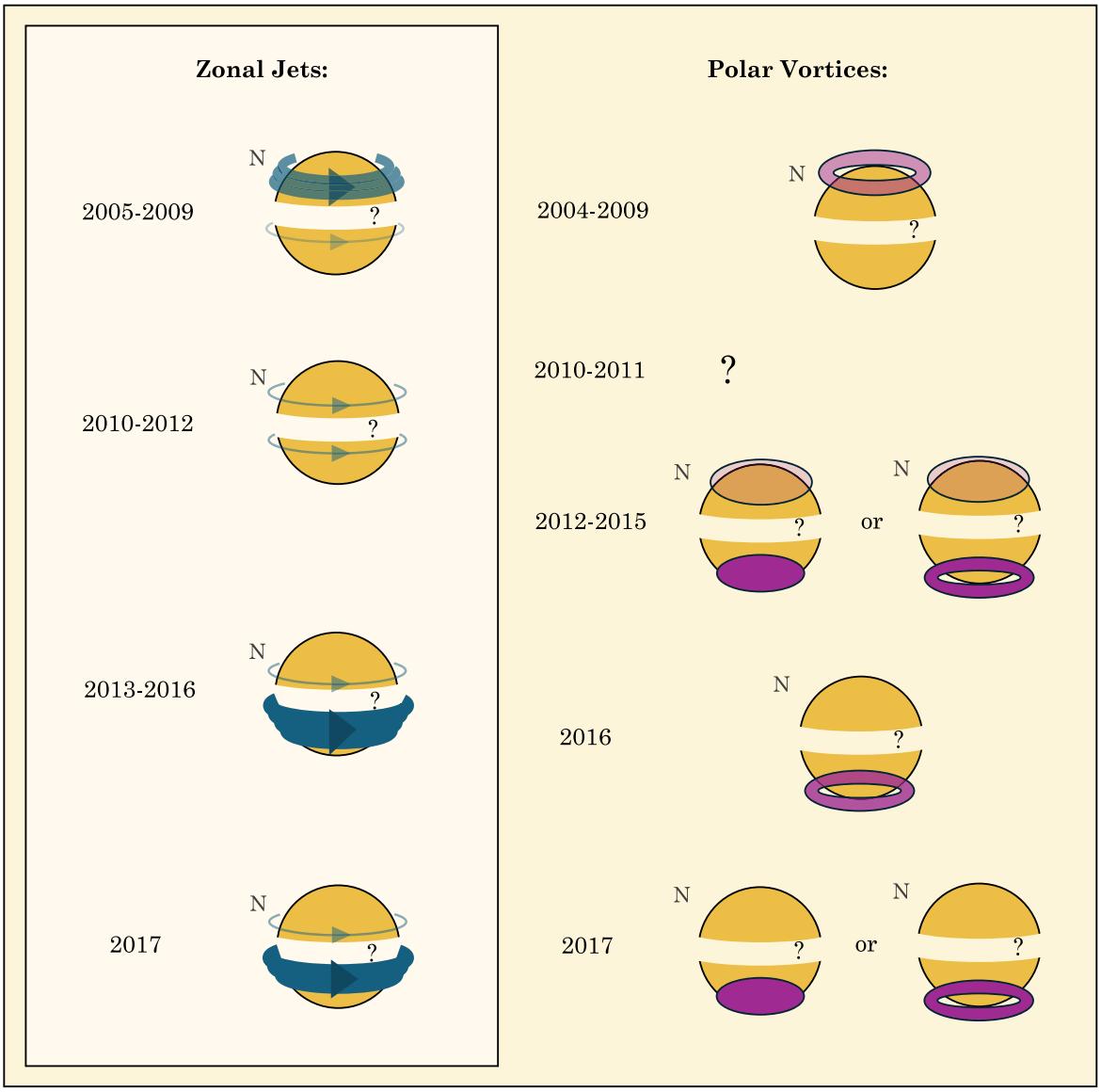

Figure 12. Schematic of zonal jets observed in the mean zonal wind field (left) and interpretation of the Lait PV structure in relation to Titan's polar vortices (right). The equatorial region is unconstrained. A purple ring indicates an annular vortex, and a solid oval indicates a conventional vortex shape. Jet and vortex strengths are indicated by color opacity: higher opacity indicates faster zonal winds (blue) or higher Lait PV (purple). Due to limited coverage of the highest latitudes, we cannot conclude whether the Lait PV structure is annular at some times.

up to 160 m s^{-1} in the south. This discrepancy is a known issue, likely related at least in part to the model's resolution and lack of trace gas and haze coupling with the circulation.

The structure of our mean zonal wind field is consistent with TAM, but with additional structure due to the higher meridional resolution we achieve. TAM predicts a single zonal jet core in the winter hemisphere. We now describe the observed evolution of the mean zonal wind structure in detail, and our interpretation is summarized in Figure 12.

5.4.3. Northern Hemisphere Wind Evolution

We observe a circumpolar jet at around 40°–50° north in northern winter (2004–09, $L_s \approx 290°$–5°) with peak speed ∼210 m s^{-1}, reducing to ∼190 m s^{-1} by 2009 ($L_s \approx 355°$–5°). This is consistent with the predicted weakening of the meridional overturning circulation (R. K. Achterberg et al. 2011) as Titan approaches northern spring equinox in 2009. Less angular momentum is transported to high northern latitudes in late northern winter, leading to weakening of the jet. The lower-latitude jet migrates equatorward and gradually reduces in speed from ∼190 m s^{-1} in 2010 ($L_s \approx 10°$) to ∼120 m s^{-1} in 2017 ($L_s \approx 90°$), consistent with J. Sharkey et al. (2021). We observe the northern zonal jet to persist until at least 2013 ($L_s \approx 45°$), although wind speeds only reach ∼135 m s^{-1}.

5.4.4. Southern Hemisphere Wind Evolution

Pre-equinox, we observe a weak zonal jet at around 20° south with peak wind speed ∼110 m s^{-1}. This has some symmetry, with the northern jet observed to persist in the northern hemisphere well after the equinox, which sits at around 25° north in 2017 ($L_s \approx 90°$). The weak spring/summer-hemisphere jet is not resolved in GCMs (C. E. Newman et al. 2011; S. Lebonnois et al. 2012;

N. A. Lombardo & J. M. Lora 2023b, 2023a). Instead, GCMs predict the main winter-hemisphere jet to extend into the summer hemisphere, for example, in the TAM model (N. A. Lombardo & J. M. Lora 2023b, 2023a; Figure 11). Previous observational studies have also predicted an extension of the northern jet into the south (e.g., R. K. Achterberg et al. 2008a; J. Sharkey et al. 2021). Our observed wind contours are subject to uncertainties and agree, within unknowns, with the previous results and simulations that there is a single jet that crosses the equator.

Immediately after the equinox (from 2009 onward, $L_s \lesssim 0°$), the weak southern jet rapidly strengthens and gradually migrates poleward, from $\sim$110 m s^{-1} at 25° south in 2009 to $\sim$230 m s^{-1} at 40° south in 2013 (Figure 11, left). This is consistent with the predicted reversal of the meridional overturning circulation that transports momentum to the southern hemisphere (S. Vinatier et al. 2020). Meanwhile, there is a suggestion that a second circumpolar jet might form at higher southern latitudes, around 70° north, first evident in 2012 ($L_s \approx 35°$). However, the robustness of this result is low given the observational noise and given that, dynamically, this configuration would be extremely unstable. Due to the instability of this configuration, we would not expect to observe multiple jets in the simulated wind field. This apparent second jet appears to descend from altitudes above the sensitive region of our observations (pressures $\gtrsim$0.001 mbar) and then gradually extend to lower altitudes, reaching 0.5 mbar in 2016 ($L_s \approx 80°$), strengthening until it reaches a peak wind speed of $\sim$230 m s^{-1} in 2015 ($L_s \approx 70°$). However, it is unclear whether this jet is increasing in speed or the fast jet core is simply descending into our probed region. The jet core simulated by the TAM GCM follows a similar descent, from around 0.1 mbar in 2011 ($L_s \approx 25°$) to 2 mbar by 2017 ($L_s \approx 90°$). Two jets in the south are observed to persist in individual observations during 2016. After 2015 ($L_s \gtrsim 65°$), we observe weakening of the southern jet, in agreement with S. Vinatier et al. (2020). The two jets appear to merge in 2017 ($L_s \approx 90°$), resulting in a single jet of speed $\sim$225 m s^{-1}.

5.4.5. Potential Temperature and Potential Vorticity

PV is a measure of rotation within large-scale atmospheric flow and combines absolute vorticity and the vertical stability of the atmosphere. It is particularly useful because it is conserved through time in the absence of frictional or diabatic forces acting on it. As such, it gives us an indication of the rotation and intensity of the polar vortices as they evolve throughout the season. The edge of the polar vortex acts as a mixing barrier, leading to confinement of trace gases at the pole (N. Teanby et al. 2006). A strong horizontal PV gradient can be evidence of the mixing barrier (D. G. Andrews 1987), as is the case at the edge of Earth's antarctic polar vortex (M. E. McIntyre & T. N. Palmer 1983; M. McIntyre 1989), so it can be used to probe a vortex edge. A steep PV gradient may also indicate the existence of atmospheric waves such as Rossby waves (B. J. Hoskins et al. 1985; E. R. Nash et al. 1996); however, Rossby waves are not expected to propagate in Titan's stratosphere (J. Sharkey et al. 2020). The redistribution of PV can be closely related to the propagation of Rossby waves, which may be important in the breakup of the polar vortex. PV distributions are therefore important in describing the structure and stability of Titan's polar vortices.

Previous studies have investigated Titan's stratospheric PV distribution (R. K. Achterberg et al. 2008b, 2011; N. A. Teanby et al. 2008; D. M. Mitchell et al. 2021; J. Sharkey et al. 2021). PV has been used previously to probe the weakening of the north polar vortex (N. A. Teanby et al. 2008; R. K. Achterberg et al. 2011; J. Sharkey et al. 2021) and the strengthening of Titan's south polar vortex (J. Sharkey et al. 2021). In these studies, there is a suggestion of an annular PV structure encircling Titan's winter pole, where a PV maximum sits at high latitudes with a local PV minimum at the winter pole. Opposing PV gradients have been shown to be barotropically unstable (D. G. Dritschel 1986; L. Rayleigh 1879), so an annular PV structure should not persist without some external restoring force. However, J. Sharkey et al. (2020) find that the north polar vortex is zonally uniform, suggesting that the vortex is largely barotropically stable. We determine the zonal mean PV distribution in Titan's stratosphere from the zonal wind field and use it to diagnose the shape and strength of the north and south winter polar vortices.

In a rotating fluid, the PV, q, describes a combination of the absolute vorticity (the local rotation of the fluid) and stratification (the vertical gradient of the potential temperature, Θ):

$$q = -g(f + \xi_\Theta)\frac{\partial \Theta}{\partial p} \tag{4}$$

(P. L. Read et al. 2006), where the potential temperature, Θ, is the temperature of an air parcel if it were moved adiabatically —that is, without loss or gain of heat—from some pressure level, p, to some reference pressure, p_0 (J. Houghton 2002),

$$\Theta = T\left(\frac{p_0}{p}\right)^{\kappa}. \tag{5}$$

The ratio of specific heat capacities $\kappa = \frac{c_p - c_v}{c_p} = 0.281$ for Titan (N. A. Teanby et al. 2008), and we use reference pressure $p_0 = 10$ mbar. The vertical component of the relative vorticity on surfaces of constant potential temperature is

$$\xi_\Theta = -\frac{1}{r^2 \cos(\phi)}\frac{\partial}{\partial \phi}(ru\cos\phi), \tag{6}$$

and $f = 2\Omega\sin\phi$ is the Coriolis parameter. We determine the PV field from the potential temperature, following Equation (4). We use a finite-difference method to approximate the derivatives:

$$\left(\frac{\partial \Theta}{\partial p}\right)_{ij} \approx \frac{\Theta_{i,j+1} - \Theta_{i,j-1}}{p_{j+1} - p_{j-1}} \tag{7}$$

and

$$\xi_{\Theta,ij} \approx -\frac{1}{r_j^2 \cos\phi_i}\frac{(r_j u_{i+1,j}\cos\phi_{i+1}) - (r_j u_{i-1,j}\cos\phi_{i-1})}{\phi_{i+1} - \phi_{i-1}} \tag{8}$$

for the ith latitude and jth pressure level, and $r_j = r(p_j)$ and $u_{ij} = u(p_j, \phi_i)$. The radial polar coordinate, $r = R_T + h$, must remain a variable in Equation (6), as Titan's deep atmosphere means that it has significant atmospheric curvature compared to its radius.

PV has a large vertical variation, due its inverse dependence on the pressure, $p_{j+1} - p_{j-1}$, so we scale the PV by factor $(\Theta/100)^n$ to reduce this variation while preserving the

horizontal structure and conservative properties of PV. This scaling was first suggested by L. R. Lait (1994), who use $n = -9/2$. We instead use $n = -7/2$, which is more appropriate for Titan's atmospheric composition (N. A. Teanby et al. 2008). Cross sections of the scaled PV magnitude are plotted against the potential temperature in Figure 13 for each Earth year. Regions where the scaled PV error exceeds the contour interval ($>5 \times 10^{-5}$ $m^2\,K\,kg^{-1}\,s^{-1}$) have been removed. The Appendix outlines how we determine the uncertainty in Lait PV. The radiative timescales in Titan's stratosphere range in length from a Titan day to a Titan season (B. Bézard et al. 2018), so PV features can persist in the stratosphere over multiple Earth years. Since PV effectively depends on the second derivative of temperature, it can be significantly influenced by fine structure in the temperature field, and although smoothing has been applied, only large-scale structure in PV should be considered reliable. The PV field is calculated from the temperature field smoothed with cubic B-splines with a knot spacing of 10°. This should preserve finer meridional structure than achieved by previous studies of the PV structure of Titan's stratosphere (R. K. Achterberg et al. 2008a, 2011; J. Sharkey et al. 2021). Our interpretation of the observed Lait PV structure in relation to Titan's polar vortices is summarized in Figure 12, and we now describe the broad structure in the determined zonal PV.

5.4.6. Northern Hemisphere Potential Vorticity Evolution

Throughout mid- to late northern winter, we observe a suggestion of an annulus of PV encircling the north pole, with a PV maximum around 60°–80° north and a local PV minimum at the north pole (Figure 13). This is consistent with N. A. Teanby et al. (2008), R. K. Achterberg et al. (2011), and J. Sharkey et al. (2021), who observe a tentative annulus of PV at around 65° north in northern midwinter. This annulus of PV persists from at least 2005 ($L_s \approx 305°$) through to the northern spring equinox in 2009 ($L_s \approx 0°$), suggesting that Titan's northern polar vortex has an annular shape for at least 5 yr leading up to equinox. The annular PV structure does not seem to be an artifact due to increasing emission angles toward the pole: local PV minima are observed in multiple individual observations with emission angles of less than 40°. Due to the limited coverage of our observations, it is unclear whether the north polar vortex has an annular shape immediately post-equinox (2010–2011). However, a weak PV gradient persists at high northern latitudes at least during 2012–2014 ($L_s \approx$ 30°–65°), and there are hints of this in 2015 and 2016 ($L_s \approx$ 65°–85°), although it is unclear whether this takes an annular shape. This is consistent with evidence for the confinement of trace species in the north polar region, which is observed to persist until 2016 (N. A. Teanby et al. 2019).

In Figure 13, there is a hint of a secondary PV annulus at higher altitudes, at pressures $\lesssim$0.1 mbar ($\Theta \sim 1000$ K), sitting persistently at around 40° north. PV is effectively the second derivative of the temperature field and is therefore very sensitive to noise in the temperature. Subtler features in the observed PV structure could be an artificial product of noise amplification in the temperature field, despite our efforts to limits this to PV through smoothing the temperature field. However, the northern secondary PV annulus is evident in almost all observation sequences that have sufficient latitude coverage in 2006 ($L_s \approx 330°$), 2008 ($L_s \approx 345°$), 2009 ($L_s \approx 0°$), and 2012–2016 ($L_s \approx$ 30°–85°).

There is a suggestive detached PV maximum low in stratosphere, around 1 mbar ($\Theta \approx 300$ K). We observe this at approximately 70° north during 2006–2009 ($L_s \approx 315°$–5°) and 2012–2014 ($L_s \approx 30°$–65°), although it significantly weakens after Titan's equinox. This feature is seen in the majority of individual observation sequences acquired during this time and is also evident in the PV structure determined from CIRS limb observations by N. A. Teanby et al. (2008) and CIRS nadir observations (J. Sharkey et al. 2021) in the northern hemisphere during northern winter. This package of PV may have been deposited by breaking gravity waves. Breaking waves can deposit energy into the zonal flow, producing an enhanced PV gradient that prevents mixing across it. This would prevent air at high northern latitudes from mixing with warmer air from the south, and thus we observe this feature as a cold spot low in the stratosphere near the north pole (Figure 10). Gravity waves have been observed in the equatorial region to propagate vertically into Titan's lower stratosphere up to at least the 3 mbar level (R. D. Lorenz et al. 2014), if not higher. Perhaps gravity waves also exist in the north polar region: topographic variations are weak on Titan (R. D. Lorenz et al. 2013), but waves could alternatively be generated by differences in surface-lake temperatures owing to the longitudinal asymmetry in lake distribution at high northern latitudes.

Regions of high meridional PV gradient can be evidence of a mixing barrier and so can diagnose the location of the vortex edge. The right panels of Figure 13 show the Lait PV on isentropic surfaces with potential temperature $\Theta = 350$, 700, and 1000 K, which correspond to approximately 1, 0.1, and 0.01 mbar in Titan's atmosphere, respectively. The north polar annulus has a width of approximately 20° at ~1 mbar ($\Theta = 350$ K; Figure 13, pink lines), with the outer edge sitting at around 60° north. At higher altitudes, ~0.1 and 0.01 mbar ($\Theta = 700$ and 1000 K; Figure 13, blue and green lines), the vortex seems to be wider, around 30°, with the outer edge sitting at ~50° north. The width of the vortex does not have a noticeable time dependence during this period, but it appears to be moving generally poleward.

5.4.7. Southern Hemisphere Potential Vorticity Evolution

From at least 2012 ($L_s \approx 35°$), we observe a large PV at high southern latitudes, which persists until at least 2016 ($L_s \approx 80°$). The PV maximum appears to sit at the south pole, although we cannot say for certain, as our observations do not extend to the pole. Near the end of the mission ($L_s \approx 80°$), the PV is observed to be annular, particularly clear in the right 2016 panel of Figure 13. It is therefore suggestive that Titan's polar vortex begins its life as a conventional vortex, a stable configuration, persisting for at least 6 yr (approximately a quarter of a Titan year) after the equinox, and then begins to transition to an annular shape, with maximum PV at ~75° south in 2016 ($L_s \approx 80°$) at 1–0.001 mbar and ~70° south in 2017 ($L_s \approx 90°$) at 0.1–0.001 mbar. This is in agreement with J. Sharkey et al. (2021), who find the PV to be maximum at the south pole in 2013 ($L_s = 42°$) and then at ~60° south in 2017 ($L_s = 86°$) at the 0.1 mbar level. The PV in the south during formation of the south polar vortex is around 4 times stronger than the maximum PV observed in the northern hemisphere during breakup of the north polar vortex, consistent with J. Sharkey et al. (2021). We would not expect to observe symmetry between the north/south vortices, as Cassini

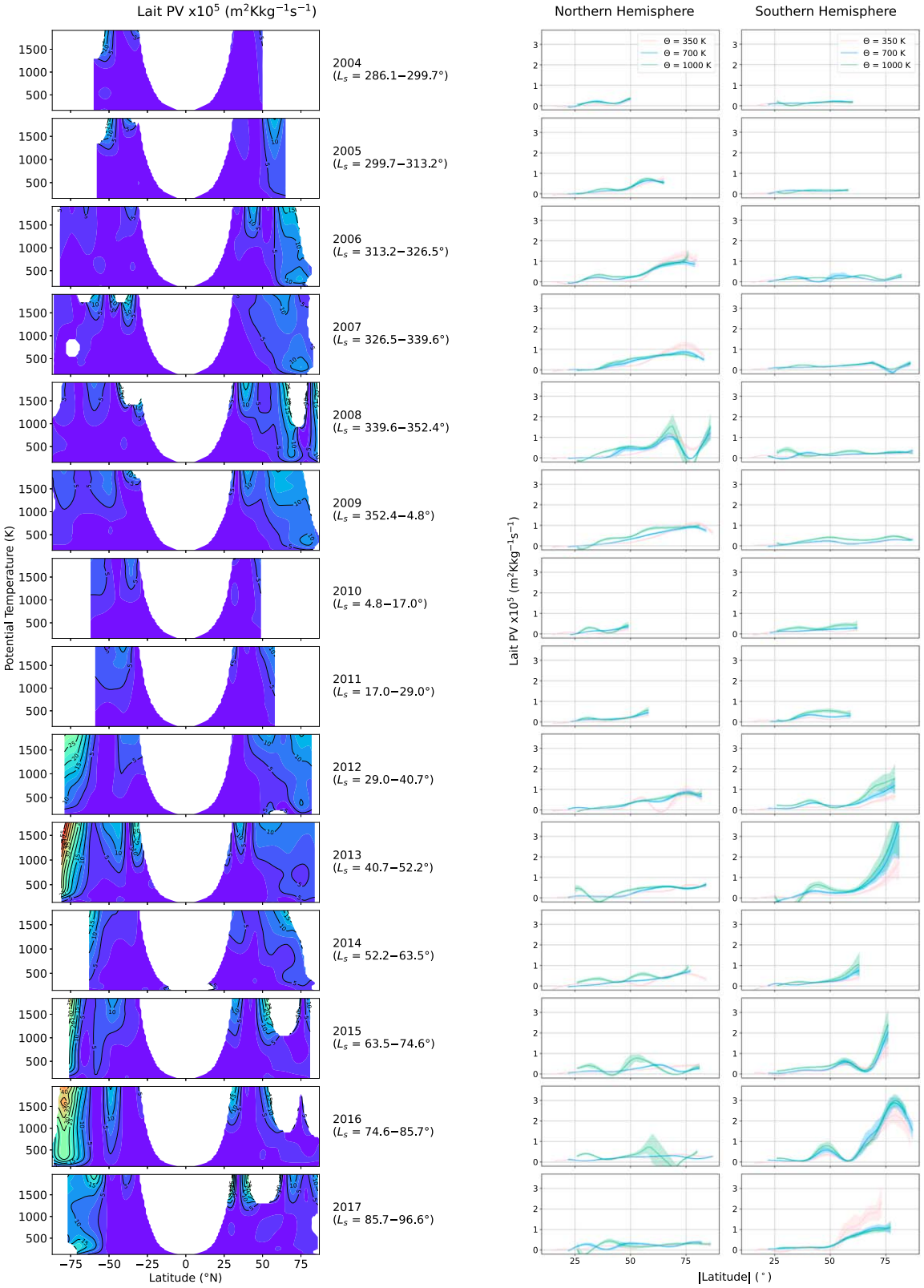

Figure 13. Scaled PV ("Lait PV" = PV $\times(\Theta/100\ \mathrm{K})^{-7/2}$) determined from observations. PV is plotted against potential temperature and is scaled by a factor of the potential temperature field, Θ, to reduce the vertical variation of PV while preserving its horizontal structure and conservative properties. PV is calculated from our zonal wind and potential temperature determined from the observed zonal mean temperature field. The PV field is calculated from the temperature field smoothed with cubic B-splines with a knot spacing of 10°. Regions where the scaled PV error exceeds the contour interval ($>5 \times 10^{-5}$ m^2 K kg^{-1} s^{-1}) have been removed. Right: Lait PV is plotted on isentropic surfaces: Θ = 350, 700, and 1000 K, which correspond to approximately 1, 0.1, and 0.01 mbar, respectively, in Titan's atmosphere (solid lines). Shaded regions show the error on the Lait PV. An additional smoothing has been applied to the Lait PV line plots (right), by fitting cubic B-splines (N. A. Teanby 2007) with a knot spacing of 5°. The sign of PV in the southern hemisphere has been inverted so that the hemispheres can be directly compared on the plot.

observed different parts of Titan's seasonal cycle for the northern/southern hemispheres.

As in the northern hemisphere, there is also a suggestion of a secondary PV annulus in the south. During 2007–2016 ($L_s \approx 330°$–$85°$), there appears to be a PV annulus in the southern midlatitudes, around 60° south: in general, migrating equatorward leading up to equinox, then poleward post-equinox. This is observed in the majority of individual observation sequences during these time frames. However, as with secondary structures in the zonal wind field, the robustness of this feature is low given the considerations of observational noise and dynamical stability. Furthermore, in the left 2017 panel of Figure 13, we see a detached PV maximum lower in the stratosphere, around 1 mbar ($\Theta \approx 300$ K), mirroring the similar PV feature observed in the northern hemisphere earlier in the mission.

Again, we examine the Lait PV on some isentropic surfaces to diagnose the vortex edge. At $\Theta = 700$ K (~0.1 mbar), the south polar vortex outer edge varies between around 65° and 75° north during its formation (2012–2017, $L_s \approx 30°$–$90°$). The outer edge of the vortex appears to migrate equatorward during this period, suggesting that the vortex is growing in size, or perhaps becoming annular if an inner edge is forming. Later, during 2016 ($L_s \approx 80°$), there is evidence of an inner edge of the vortex, as we observe a negative meridional PV gradient at latitudes south of 80° south, suggesting an annular shape, which appears to continue to migrate equatorward during 2016–2017. The gradient of the PV in the south is significantly larger than in the north, suggesting that the (forming) south polar vortex edge acts as a stronger mixing barrier than the edges of the (decaying) north polar vortex, in agreement with J. Sharkey et al. (2021) and the observed isolation of species at the winter pole (e.g., N. A. Teanby et al. 2019; S. Vinatier et al. 2020). Composition mapping in the stratosphere suggests that there are no significant differences between the north and south polar vortices (J. Sharkey et al. 2021). However, the eccentricity of Saturn's orbit means that Titan's southern winter receives more insolation and is longer than the northern winter, so there may be asymmetry between Titan's northern and southern polar vortices. To build up a complete picture of Titan's winter polar vortex behavior, observations spanning the second half of Titan's year ($L_s = 93°$–$293°$), not covered by Cassini, would be required. Due to geometry, ground-based observatories are unable to observe Titan's winter polar region, highlighting the importance of a Titan polar orbiter to observe the polar vortices (C. A. Nixon et al. 2020; J. W. Barnes et al. 2021).

The meridional extent of the south polar vortex is observed to be larger at higher altitudes during 2012–2015 ($L_s \approx 30°$–$75°$; Figure 13). This equatorward tilt in PV with increasing altitude has previously been observed in the PV structure of the polar vortices on Titan (J. Sharkey et al. 2021), Earth, and Mars. However, the PV feature tilts poleward as opposed to equatorward on Mars (D. M. Mitchell et al. 2015). The PV altitude tilt seen on Earth and Mars has been attributed to gravity waves (D. M. Mitchell et al. 2015). N. W. Kutsop et al. (2022) observe circumpolar haze bands in Titan's stratosphere at altitudes of $\gtrsim$100 km ($\lesssim$8 mbar) using Cassini/VIMS observations. At the 1 mbar level ($\Theta = 350$ K; Figure 13, pink lines), we observe hints of secondary PV maxima at similar latitudes to where the haze bands are observed. In the northern hemisphere during 2012–2017 ($L_s \approx 30°$–$90°$), we observe hints of local PV maxima broadly around 25°, 50°, and 75° north; however, again, these features should be interpreted with caution. N. W. Kutsop et al. (2022) suggest that haze bands form owing to haze particles being transported with the meridional circulation and collecting at mixing barriers. Our observed PV structure—that is, opposing PV gradients, which can act as barriers to mixing—suggest that such mixing barriers do indeed exist, confining the haze in bands. Alternatively, the enrichment of haze in these bands might affect the absorption of solar radiation, impacting the local temperature structure, circulation, and hence the PV structure. For example, temperature changes may generate atmospheric waves, affecting the PV structure, since PV is also a diagnostic of Rossby waves (B. J. Hoskins et al. 1985; E. R. Nash et al. 1996). There could be a positive feedback between the confinement of haze and the observed PV structure. Higher-resolution models and observations would be required to determine whether these observed PV features, including secondary PV annuli and the detached lower-stratosphere PV maximum, are real. Models may also require additional processes, for example, radiatively active tracer species, to fully understand the physical mechanisms responsible.

5.4.8. Significance for the Dragonfly Mission

The Dragonfly mission is forecast to launch in 2028 and arrive at Titan in the mid-2030s. Before beginning operation at Titan's surface, Dragonfly must undergo a parachute descent through Titan's superrotating middle atmosphere without damage. Zonal winds have a significant impact on Dragonfly's landing ellipse (the area where Dragonfly is expected to land; R. D. Lorenz 2021). The east–west dimension of the ellipse largely depends on the uncertainty in the zonal wind field (R. D. Lorenz et al. 2021). Furthermore, due to the strength of Titan's zonal winds, the stratospheric tilt is a major component of the meridional wind field, so the north–south dimension of the landing ellipse is dependent on the stratospheric tilt axis. Improved knowledge of the tilt at the time and location of Dragonfly's descent will better inform the north–south dimension of the landing ellipse.

The north–south size of the ellipse is dependent on the uncertainty in the tilt offset. Consideration of the tilt offset could shift the predicted landing location of Dragonfly by around 2–3 km (R. D. Lorenz, in private communication), which should land near the Selk impact crater at around 7° north, 199° west (R. D. Lorenz et al. 2021). Dragonfly is planned to arrive at Titan in 2035 in late northern winter ($L_s \approx 310°$). This coincides with the season observed early in the Cassini mission, which arrived at $L_s = 293°$. The stratosphere at Dragonfly's arrival is therefore expected to be similar to our 2005 panel in Figures 10 and 11. Assuming that the stratospheric tilt direction is fixed in the inertial frame, we can predict that the tilt axis will be within the uncertainty envelope $\psi = 114°$–$125°$ (3σ error) west of the subsolar point at northern spring equinox. The magnitude of the tilt is more complicated. In the inertial-fixed frame, we determine the tilt to fluctuate. There is a suggestive seasonal trend in the tilt magnitude (Figure 8), so we loosely predict the tilt to have a similar magnitude at the same point in the next seasonal cycle. Therefore, it might be expected that the tilt during 2035, $L_s \sim 310°$, will be similar to the tilt in 2005 ($L_s \sim 310°$), which

is $\beta = 2.^{\circ}7 \pm 1.^{\circ}1$. However, with only half a Titan year of coverage, this seasonal trend is tentative, and for mission planning purposes a conservative estimate of the tilt would be $\beta = 0.^{\circ}2$–$10.^{\circ}0$.

6. Conclusions

Using 85 Cassini/CIRS nadir observation sequences, spanning almost half a Titan year ($L_s = 293°$–$93°$), we present the highest meridional resolution study of Titan's stratospheric zonal mean temperature field to date. We find strong evidence that the direction of Titan's stratospheric tilt axis is constant in the inertial-fixed (solar-system-fixed) reference frame and thus is unlikely caused by Saturn gravitational forcing or solar forcing. The mean tilt axis in the inertial-fixed frame is determined to be $\beta = 4.^{\circ}0 \pm 0.^{\circ}4$ directed $\psi = 120° \pm 6°$ west of the subsolar point at northern spring equinox. Furthermore, the magnitude of the tilt axis appears to have a seasonal dependence in the solar- and inertial-fixed frames, with the maximum and minimum tilt appearing to lag the equinox and solstice, respectively, by 2–3 Earth years.

We resolve a midlatitude zonal jet, with a maximum speed of $210 \pm 10\,\mathrm{m\,s^{-1}}$ in the northern hemisphere during northern winter and $230 \pm 10\,\mathrm{m\,s^{-1}}$ in the southern hemisphere during southern spring, consistent with previous studies (S. Vinatier et al. 2020; J. Sharkey et al. 2021). There is a suggestion that multiple zonal jets might exist at some times during Titan's seasonal cycle: one or two strong jets in the winter hemisphere and one weak jet persisting in the summer hemisphere, although the robustness of this result is low given dynamical considerations and the observational noise. By using observations spanning almost half a Titan year, we are able to observe the breakup of Titan's north polar vortex and the formation of the south polar vortex. The south polar vortex appears to become annular as southern winter approaches, as is observed for the north polar vortex in northern winter. These observations provide strong motivation for future high-resolution GCM studies. Improved knowledge of the zonal wind structure in Titan's middle atmosphere and refined constraints on the stratospheric tilt axis may support landing calculations for the upcoming Dragonfly mission (R. D. Lorenz 2021; R. D. Lorenz et al. 2021).

Acknowledgments

This work was funded by the UK Science and Technology Facilities Council (STFC), grant Nos. ST/W507325/1 (L.W.) and ST/Y000676/1 (N.A.T.). C.A.N. was supported by NASA's Solar System Observations (SSO) Program and GSFC's Strategic Science initiative. N.A.L. and J.M.L. were funded by NASA CDAP grant 80NSSC20K0483.

Data Availability

Cassini CIRS data were obtained from the Planetary Data System (PDS; C. Nixon 2011).

Software: We use the NEMESIS general-purpose radiative transfer and retrieval code (P. Irwin et al. 2008) (https://github.com/nemesiscode/radtrancode).

Appendix
Uncertainty in Zonal Wind and PV

Here we outline how we estimate the uncertainty in the zonal wind speed and Lait PV. The uncertainty in the retrieved temperature is propagated through the TWE.

For a function $f(x, y, \ldots)$, where $x, y, \ldots$ have errors $\sigma_x, \sigma_y, \ldots$, respectively, the error, σ_f, on f is given by

$$\sigma_f^2 = \left(\frac{\partial f}{\partial x}\right)^2 \sigma_x^2 + \left(\frac{\partial f}{\partial y}\right)^2 \sigma_y^2 + \ldots \tag{A1}$$

(H. J. C. Berendsen 2011). Given this and Equations (3), (7), and (8), the uncertainty, $\sigma_{u,i,j}$, in the zonal wind velocity, $u_{i,j}$, at the ith latitude and jth pressure level in Titan's stratosphere is determined by

$$\sigma_{u,i,j}^2 = \left(\frac{\partial u}{\partial T_{i+1,j}}\right)^2 \sigma_{T,i+1,j}^2 + \left(\frac{\partial u}{\partial T_{i-1,j}}\right)^2 \sigma_{T,i-1,j}, \tag{A2}$$

where $\sigma_{T,i,j}$ is the error on temperature T_{ij}. Following Equation (4), the uncertainty, σ_q, in PV, q, is determined by

$$\sigma_{q,i,j}^2 = \left(\frac{\partial q}{\partial \Theta_{i,j+1}}\right)^2 \sigma_{\Theta,i,j+1}^2 + \left(\frac{\partial q}{\partial \Theta_{i,j-1}}\right)^2 \sigma_{\Theta,i,j-1}^2 + \left(\frac{\partial q}{\partial u_{i+1,j}}\right)^2 \sigma_{u,i+1,j} + \left(\frac{\partial q}{\partial u_{i-1,j}}\right)^2 \sigma_{u,i-1,j}, \tag{A3}$$

where $\sigma_{\Theta,i,j}$ is the error on the potential temperature, Θ_{ij}. Given that "Lait PV" = PV $\times$ $(\Theta/100\,\mathrm{K})^{-7/2}$), the uncertainty, $\sigma_{q,\mathrm{Lait}}$, in the Lait PV, q_{Lait} is determined by

$$\sigma_{q,\mathrm{Lait}}^2 = \left(\frac{\partial q_{\mathrm{Lait},i,j}}{\partial \Theta_{i,j}}\right)^2 \sigma_{\Theta,i,j}^2 + \left(\frac{\partial q_{\mathrm{Lait},i,j}}{\partial q_{i,j}}\right)^2 \sigma_{q,i,j}^2. \tag{A4}$$

ORCID iDs

Lucy Wright https://orcid.org/0000-0002-6023-5755
Nicholas A. Teanby https://orcid.org/0000-0003-3108-5775
Patrick G. J. Irwin https://orcid.org/0000-0002-6772-384X
Conor A. Nixon https://orcid.org/0000-0001-9540-9121
Nicholas A. Lombardo https://orcid.org/0000-0001-8621-6520
Juan M. Lora https://orcid.org/0000-0001-9925-1050
Daniel Mitchell https://orcid.org/0000-0002-0117-3486

References

Achterberg, R. K. 2023, PSJ, 4, 140
Achterberg, R. K., Conrath, B., Gierasch, P. J., Flasar, F. M., & Nixon, C. A. 2008a, Icar, 197, 549
Achterberg, R. K., Conrath, B. J., Gierasch, P. J., Flasar, F. M., & Nixon, C. A. 2008b, Icar, 194, 263
Achterberg, R. K., Gierasch, P. J., Conrath, B. J., Flasar, F. M., & Nixon, C. A. 2011, Icar, 211, 686
Andrews, D. G. 1987, RSPTA, 323, 693
Barnes, J. W., Hayes, A. G., Soderblom, J. M., et al. 2021, BAAS, 53, 317
Berendsen, H. J. C. 2011, A Student's Guide to Data and Error Analysis (Cambridge: Cambridge Univ. Press)
Bézard, B., Vinatier, S., & Achterberg, R. K. 2018, Icar, 302, 437
Bird, M. K., Allison, M., Asmar, S. W., et al. 2005, Natur, 438, 800
Colaprete, A., Barnes, J. R., Haberle, R. M., & Montmessin, F. 2008, P&SS, 56, 150
Cordiner, M. A., Garcia-Berrios, E., Cosentino, R. G., et al. 2020, ApJL, 904, L12

Coustenis, A., Achterberg, R. K., Conrath, B. J., et al. 2007, Icar, 189, 35
Coustenis, A., Jennings, D. E., Nixon, C. A., et al. 2010, Icar, 207, 461
Delahaye, T., Armante, R., Scott, N., et al. 2021, JMoSp, 380, 111510
Dobrijevic, M., Hébrard, E., Loison, J., & Hickson, K. 2014, Icar, 228, 324
Dritschel, D. G. 1986, JFM, 172, 157
Flasar, F. M., Achterberg, R. K., Conrath, B. J., et al. 2005, Sci, 308, 975
Flasar, F. M., Kunde, V. G., Abbas, M. M., et al. 2004, SSRv, 115, 169
Folkner, W. M., Asmar, S. W., Border, J. S., et al. 2006, JGRE, 111, 2005JE002649
Gordon, I., Rothman, L., Hargreaves, R., et al. 2022, JQSRT, 277, 107949
Hoskins, B. J., McIntyre, M. E., & Robertson, A. W. 1985, QJRMS, 111, 877
Houghton, J. 2002, The Physics of Atmospheres (Cambridge: Cambridge Univ. Press)
Houghton, J. T., Taylor, F. W., & Rodgers, C. D. 1984, Remote Sounding of Atmospheres (Cambridge: Cambridge Univ. Press)
Hourdin, F., Talagrand, O., Sadourny, R., et al. 1995, Icar, 117, 358
Irwin, P., Teanby, N., de Kok, R., et al. 2008, JQSRT, 109, 1136
Jennings, D. E., Flasar, F. M., Kunde, V. G., et al. 2017, ApOpt, 56, 5274
Kunde, V. G., Ade, P. A. R., Barney, R. D., et al. 1996, Proc. SPIE, 162, 177
Kutsop, N. W., Hayes, A. G., Corlies, P. M., et al. 2022, PSJ, 3, 114
Lacis, A. A., & Oinas, V. 1991, JGR, 96, 9027
Lait, L. R. 1994, JAtS, 51, 1754
Lavvas, P., Coustenis, A., & Vardavas, I. 2008, P&SS, 56, 67
Lebonnois, S., Burgalat, J., Rannou, P., & Charnay, B. 2012, Icar, 218, 707
Lellouch, E., Bézard, B., Flasar, F., et al. 2014, Icar, 231, 323
Lellouch, E., Gurwell, M. A., Moreno, R., et al. 2019, NatAs, 3, 614
Lewis, N. T., Lombardo, N. A., Read, P. L., & Lora, J. M. 2023, PSJ, 4, 149
Light, S., Gurwell, M., Thelen, A., Lombardo, N. A., & Nixon, C. 2024, PSJ, 5, 98
Loison, J., Hébrard, E., Dobrijevic, M., et al. 2015, Icar, 247, 218
Lombardo, N. A., & Lora, J. M. 2023a, Icar, 390, 115291
Lombardo, N. A., & Lora, J. M. 2023b, JGRE, 128, e2023JE008061
Lora, J. M., Lunine, J. I., & Russell, J. L. 2015, Icar, 250, 516
Lorenz, R. D. 2021, AdSpR, 67, 2219
Lorenz, R. D., MacKenzie, S. M., Neish, C. D., et al. 2021, PSJ, 2, 24
Lorenz, R. D., Stiles, B. W., Aharonson, O., et al. 2013, Icar, 225, 367
Lorenz, R. D., Young, L. A., & Ferri, F. 2014, Icar, 227, 49
Marcus, P. S., Tollefson, J., Wong, M. H., & de Pater, I. 2019, Icar, 324, 198
Mathé, C., Vinatier, S., Bézard, B., et al. 2020, Icar, 344, 113547
McIntyre, M. 1989, JATP, 51, 29
McIntyre, M. E., & Palmer, T. N. 1983, Natur, 305, 593
Mitchell, D. M., Montabone, L., Thomson, S., & Read, P. L. 2015, QJRMS, 141, 550
Mitchell, D. M., Scott, R. K., Seviour, W. J. M., et al. 2021, RvGeo, 59, e2020RG000723
Moreno, R., Marten, A., & Hidayat, T. 2005, A&A, 437, 319
Nash, E. R., Newman, P. A., Rosenfield, J. E., & Schoeberl, M. R. 1996, JGRD, 101, 9471
Newman, C. E., Lee, C., Lian, Y., Richardson, M. I., & Toigo, A. D. 2011, Icar, 213, 636
Niemann, H. B., Atreya, S. K., Demick, J. E., et al. 2010, JGR, 115, E12006
Nixon, C. 2011, Cassini JupiterEncounter Composite Infrared Spectrometer Data, CO-S-CIRS-2/3/4-TSDR-V3.1, NASA Planetary Data System, doi:10.17189/j98x-ag08
Nixon, C. A. 2024, ESC, 8, 406
Nixon, C. A., Abshire, J., Ashton, A., et al. 2020, arXiv:2008.05680
Nixon, C. A., Ansty, T. M., Lombardo, N. A., et al. 2019, ApJS, 244, 14
Nixon, C. A., Kaelberer, M. S., Gorius, N., CIRS Instrument Team, et al. 2014, User Guide to the PDS Dataset for the Cassini Composite Infrared Spectrometer (CIRS), https://ntrs.nasa.gov/citations/20120013660
Rannou, P., Coutelier, M., Rey, M., & Vinatier, S. 2022, A&A, 666, A140
Rannou, P., Coutelier, M., Rivière, E., et al. 2021, ApJ, 922, 239
Rannou, P., Hourdin, F., McKay, C., & Luz, D. 2004, Icar, 170, 443
Rayleigh, L. 1879, Proc. Lond. Math. Soc., s1-11, 57
Read, P. L. 1986, QJRMS, 112, 253
Read, P. L., Gierasch, P. J., Conrath, B. J., et al. 2006, QJRMS, 132, 1577
Read, P. L., & Lebonnois, S. 2018, AREPS, 46, 175
Rodgers, C. D. 1976, RvGeo, 14, 609
Roman, M. T., West, R. A., Banfield, D. J., et al. 2009, Icar, 203, 242
Sharkey, J., Teanby, N. A., Sylvestre, M., et al. 2020, Icar, 337, 113441
Sharkey, J., Teanby, N. A., Sylvestre, M., et al. 2021, Icar, 354, 114030
Sicardy, B., Colas, F., Widemann, T., et al. 2006, JGRE, 111, 2005JE002624
Snell, C., & Banfield, D. 2024, PSJ, 5, 12
Sylvestre, M., Teanby, N., Vatant d'Ollone, J., et al. 2020, Icar, 344, 113188
Teanby, N., De Kok, R., & Irwin, P. 2009a, Icar, 204, 645
Teanby, N., Irwin, P., & de Kok, R. 2010, P&SS, 58, 792
Teanby, N., Irwin, P., De Kok, R., et al. 2009b, Icar, 202, 620
Teanby, N., Irwin, P., Dekok, R., et al. 2006, Icar, 181, 243
Teanby, N. A. 2007, MatG, 39, 419
Teanby, N. A., Bézard, B., Vinatier, S., et al. 2017, NatCo, 8, 1586
Teanby, N. A., de Kok, R., Irwin, P. G. J., et al. 2008, JGR, 113, E12003
Teanby, N. A., Irwin, P. G. J., Nixon, C. A., et al. 2012, Natur, 491, 732
Teanby, N. A., Sylvestre, M., Sharkey, J., et al. 2019, GeoRL, 46, 3079
Thelen, A. E., Nixon, C. A., Cordiner, M. A., et al. 2024, PSJ, 5, 125
Tokano, T. 2010, P&SS, 58, 814
Vashist, A. S., Heslar, M. F., Barnes, J. W., Hennen, C., & Lorenz, R. D. 2023, PSJ, 4, 118
Vinatier, S., Bézard, B., Lebonnois, S., et al. 2015, Icar, 250, 95
Vinatier, S., Bézard, B., Nixon, C. A., et al. 2010, Icar, 205, 559
Vinatier, S., Mathé, C., Bézard, B., et al. 2020, A&A, 641, A116
Vuitton, V., Yelle, R., Klippenstein, S., Hörst, S., & Lavvas, P. 2019, Icar, 324, 120
West, R. A., Del Genio, A. D., Barbara, J., et al. 2016, Icar, 270, 399
Wilson, E. H. 2004, JGR, 109, E06002
Wright, L., Teanby, N. A., Irwin, P. G. J., & Nixon, C. A. 2024, ExA, 57, 15